

Fast Bayesian Functional Principal Components Analysis

Joseph Sartini ^{*1}, Xinkai Zhou¹, Liz Selvin², Scott Zeger¹, and Ciprian M. Crainiceanu¹

¹Department of Biostatistics, Johns Hopkins University

²Department of Epidemiology, Johns Hopkins University

December 17, 2024

Abstract

Functional Principal Components Analysis (FPCA) is one of the most successful and widely used analytic tools for exploration and dimension reduction of functional data. Standard implementations of FPCA estimate the principal components from the data but ignore their sampling variability in subsequent inferences. To address this problem, we propose the Fast Bayesian Functional Principal Components Analysis (Fast BayesFPCA), that treats principal components as parameters on the Stiefel manifold. To ensure efficiency, stability, and scalability we introduce three innovations: (1) project all eigenfunctions onto an orthonormal spline basis, reducing modeling considerations to a smaller-dimensional Stiefel manifold; (2) induce a uniform prior on the Stiefel manifold of the principal component spline coefficients via the polar representation of a matrix with entries following independent standard Normal priors; and (3) constrain sampling using the assumed FPCA structure to improve stability. We demonstrate the application of Fast BayesFPCA to characterize the variability in mealtime glucose from the Dietary Approaches to Stop Hypertension for Diabetes Continuous Glucose Monitoring (DASH4D CGM) study. All relevant STAN code and simulation routines are available as supplementary material.

Keywords: Bayesian Methods, Functional Data, Computationally Intensive Methods, Uncertainty Quantification, Semiparametric Methods

^{*}DASH4D Trial is funded by a grant from the Sheikh Khalifa Stroke Institute at Johns Hopkins University School of Medicine. The DASH4D-CGM study is funded by NIH/NIDDK grant R01 DK128900. Dr. Selvin was also supported by NIH/NHLBI grant K24 HL152440. Mr. Sartini was supported by Grant Number T32 HL007024 from the National Heart, Lung, and Blood Institute, National Institutes of Health. The content is solely the responsibility of the authors and does not necessarily represent the official views of the National Institutes of Health. Abbott Diabetes Care provided continuous glucose monitoring systems for this investigator-initiated research.

1 Introduction

Functional principal component analysis is a first line analytic approach in high-dimensional applications where there is an underlying assumption that the data varies smoothly over some domain(s). The standard implementation relies on diagonalizing the covariance operator estimated using the observed data, followed by inference conditional on the functional principal components (FPCs) [8]. This implicitly assumes that FPCs do not have any sampling error variability, an assumption invalidated by resampling the data. Whether this assumption affects downstream inferences remains an open question and requires extensive further analyses in specific applications.

We propose a model where the FPCs are treated as random variables. Because the eigenfunctions are orthonormal, their natural parameter space is the Stiefel manifold, the space of matrices with orthonormal columns. We design a Bayesian algorithm to efficiently sample this parameter space using a novel combination of 3 components: (1) project all eigenfunctions onto an orthonormal spline basis to reduce dimensionality - the coefficient matrix will lie on a lower dimensional Stiefel manifold if and only if the original data principal components lie on a higher dimensional Stiefel manifold; (2) induce a uniform prior on the Stiefel manifold of the principal component spline coefficients, representing a subspace of smooth functions at the original data scale, using the polar decomposition; and (3) leverage ordered objects in STAN and reasonable initial estimates of fixed effects and variance components to appropriately initialize sampling. These aspects are the key elements of our fast, stable, and scalable Bayesian algorithm, implemented in reproducible software.

Fast BayesFPCA is part of an expanding literature that treats principal components as unknown parameters. One of the first attempts used a frequentist approach and likelihood optimization over the Stiefel manifold [26] but did not account for uncertainty in the eigenfunctions. A fully Bayesian implementation of FPCA was proposed in [16] using spline expansion to smooth functional components and post-processing to obtain the posterior distributions of the eigenfunctions. More recently, [20] modeled the data using the Singular Value Decomposition (SVD) on the original data space, combined with polar decomposition and matrix normal priors to induce orthonormality and smoothness of the functional principal components in the original data space. This method is more closely related to Fast BayesFPCA; however, it uses a higher dimensional Stiefel manifold of eigenfunctions on the original space, whereas we use a lower dimensional Stiefel manifold of eigenfunctions in a spline coefficients space. The publication [37] proposed an approach related to that of [20], though they induced smoothing of the eigenfunctions by modeling the spline coefficients and their implementation was based on Gibbs sampling. At the time of writing this paper, no software is available for the method described in [37]. As we were submitting this paper, [24] put forward an extensible variational Bayes approach to FPCA

with supporting software. Among these implementations, Fast BayesFPCA uniquely leverages the combination of Polar decomposition and orthogonal spline expansion to induce a uniform prior on the low dimensional Stiefel manifold of spline coefficients.

This research is motivated by a study goal of the Dietary Approaches to Stop Hypertension for Diabetes Continuous Glucose Monitoring (DASH4D CGM) clinical trial. DASH4D CGM was a crossover feeding trial which also collected meal timing data for a subset of 65 participants, producing a total of 768 meals divided between 4 diets. For the purposes of distributing meals and collecting biomarker data, participants visited the study site and ate meals there 3 times per week. Study staff recorded the start times for these meals where possible. We evaluated mealtime (pre- and post-prandial) responses using CGM data collected during the observed mealtimes. It is crucial to characterize these responses, as postprandial glucose is an important marker of metabolic insulin responsiveness known to be associated with adverse cardiovascular outcomes [18, 14, 2, 32].

Analyses of postprandial CGM glucose with verified mealtimes are rare, and previous studies focused primarily on data taken at a small number of time points after the meal [28, 3]. We instead examine five-hour CGM curves beginning one hour before and ending four hours after each meal. Because the main results of the trial are not yet published, this paper characterizes the variability in the observed curves by diet rather than examining the expected treatment effects. We apply FPCA to the CGM curves aggregated by participant and MFPCA to the raw meal responses within each diet to conduct these analyses. The number of participants in this study is relatively small because of the costs associated with the data collection. Therefore, the estimated principal components will be estimated with substantial variability, potentially impacting downstream analyses. Here we propose to quantify the effects of this variability on statistical inferences of interest.

The rest of the paper is organized as follows. Section 2 presents the model and the full conditionals for Fast BayesFPCA. Section 3 provides the `STAN` code used to efficiently sample the posterior distribution of all parameters given the observed data. Section 4 compares the accuracy, validity, and efficiency of Fast BayesFPCA with existing implementations [16] and [20] in two simulation scenarios. Section 5 details the results of applying Fast BayesFPCA to the motivating data from the DASH4D clinical trial. Section 6 is the discussion.

2 Methods

The data structure is of the form $Y_i(t), i = 1, \dots, N, t \in T = \{t_1, \dots, t_M\} \subset [T_L, T_R]$, where T could be time or any other functional domain observed over compact interval $[T_L, T_R]$. Below we describe the model structure, priors, and full conditionals for Fast BayesFPCA.

2.1 Conditional likelihood

The Gaussian FPCA model is

$$Y_i(t) = \mu(t) + \sum_{k=1}^{\infty} \xi_{ik} \phi_k(t) + \epsilon_i(t) \approx \mu(t) + \sum_{k=1}^K \xi_{ik} \phi_k(t) + \epsilon_i(t), \quad (1)$$

where $\mu(t)$ is the population mean, $\phi_k(t)$, $k = 1, \dots, K$, are orthonormal eigenfunctions of the covariance operator of $Y_i(t)$, $\xi_{ik} \sim N(0, \lambda_k)$, λ_k are the eigenvalues corresponding to $\phi_k(t)$, $\epsilon_i(t) \sim N(0, \sigma^2)$ is the error process, and $\epsilon_i(t)$ and $\phi_k(t)$ are mutually uncorrelated over i and k . For the purpose of this paper the number of principal components, K , is fixed. The model can and will be expanded, but this initial formulation will be used for building up the infrastructure for a wide variety of related models.

Model (1) is well known in the literature and is a first line approach to analysis of high dimensional data, with or without a functional structure [9]. This is because in many applications $K \ll M$ such that model (1) produces a low dimensional approximation of the original data. Moreover, note that conditional on the eigenvectors $\phi_k(\cdot)$, the model is a simple Gaussian random effects model. We consider instead the case when $\phi_k(t)$ themselves are unknown, are treated as parameters in a Bayesian model, and have their own associated prior and posterior uncertainty. There is inherent sampling variability encountered when estimating the $\phi_k(t)$ components which could be substantial, potentially negatively impacting downstream analyses if not appropriately accounted for. We will show that in the associated Bayesian model all full conditionals are straightforward to simulate except for those of $\phi_k(\cdot)$. *The difficulty lies in simulating this full conditional in a way that is computationally efficient, scalable and stable across simulations and applications.*

2.2 Priors

We expand both the mean function and eigenfunctions using the same orthonormal spline basis, which can be derived through orthogonalization of any standard spline basis. Let \mathbf{B} be the $M \times Q$ matrix representation of the Q dimensional orthonormal spline basis, where $Q \geq K$. Each column of \mathbf{B} corresponds to a spline basis and each row corresponds to a sampling point. Because we use an orthonormal spline basis, $\mathbf{B}^t \mathbf{B} = I_Q$, the identity matrix of dimension Q . If $\mu = \{\mu(t_1), \dots, \mu(t_M)\}^t$ and $\phi_k = \{\phi_k(t_1), \dots, \phi_k(t_M)\}^t$ are $M \times 1$ dimensional vectors, the spline expansions have the form $\mu = \mathbf{B} w_\mu$ and $\phi_k = \mathbf{B} \psi_k$, where w_μ , and ψ_k are $Q \times 1$ dimensional vectors of spline coefficients.

Denote by $\Phi = [\phi_1 | \dots | \phi_K]$ the $M \times K$ dimensional matrix obtained by column binding the $M \times 1$ dimensional vectors ϕ_k and by $\Psi = [\psi_1 | \dots | \psi_K]$ the $Q \times K$ dimensional matrix of parameters obtained by column binding the $Q \times 1$ dimensional vectors ψ_k . As $\Phi = \mathbf{B} \Psi$ it follows that $\Phi^t \Phi = \Psi^t \mathbf{B}^t \mathbf{B} \Psi = \Psi^t \Psi$ because, by construction, $\mathbf{B}^t \mathbf{B} = I_Q$. Therefore, $\Phi^t \Phi = \Psi^t \Psi$ indicating that the eigenfunctions on the original high-dimensional

space of the data, ϕ_k , are orthonormal if and only if the vectors of parameters in the low dimensional space of spline coefficients, ψ_k , are orthonormal. We thus reduce the problem of sampling high, M -dimensional orthonormal eigenvectors to one of sampling low Q -dimensional parameters of an orthonormal spline basis. This is a crucial observation that will have substantial implications for the implementation of Fast BayesFPCA.

We add smoothing priors for both the mean $\mu(t)$ and eigenfunctions $\phi_k(t)$ using posterior penalties of the type $\alpha \int f^2(t)dt + (1-\alpha) \int \{f''(t)\}^2 dt$, where $f(\cdot)$ denotes a generic function. This penalty, used in [16], contains fixed weighting parameter α , and $\alpha = 0$ corresponds to the famous penalized spline prior [10, 25]. If $f(t) \approx B(t)\theta$, then the penalty is a quadratic function of the parameters θ . There exist unique and specific penalty matrices $\mathbf{P}_0, \mathbf{P}_2$ such that $\int f^2(t)dt \approx \theta^t \mathbf{P}_0 \theta$ and $\int \{f''(t)\}^2 dt \approx \theta^t \mathbf{P}_2 \theta$ [10, 22, 25, 33]. We follow [16] and define $\mathbf{P}_\alpha = \alpha \mathbf{P}_0 + (1-\alpha) \mathbf{P}_2$. Using this notation, we find that $\alpha \int f^2(t)dt + (1-\alpha) \int \{f''(t)\}^2 dt \approx \theta^t \mathbf{P}_\alpha \theta$. We use this mixed penalty with $\alpha = 0.1$ for consistency with existing implementations, as they are unable handle the singular $\alpha = 1$ case. However, note that Fast BayesFPCA does not have this restriction. For more details on this singular penalty, see for example [9, 35]. See the Supplement Section S1 for the matrix form of \mathbf{P}_α .

As this is common knowledge in statistics, we will only underline the connection of this penalty with a normal Bayesian prior [4, 27, 35] on the parameters θ of the function $f(\cdot)$. This is equivalent to assuming the following Normal priors for the mean and principal components spline parameters, respectively

$$w_\mu \propto \exp \left\{ -\frac{h_\mu}{2\sigma^2} w_\mu^t \mathbf{P}_\alpha w_\mu \right\}, \quad \psi_k \propto \exp \left\{ -\frac{h_k}{2\sigma^2} \psi_k^t \mathbf{P}_\alpha \psi_k \right\},$$

where $h_\mu > 0$ and $h_k > 0$ are different smoothing parameters. The first distribution can be viewed as a $N(0, 2\sigma^2/h_\mu \mathbf{P}_\alpha^{-1})$. The same applies to the k smoothing priors for ψ_k . Here each eigenfunction has its own smoothing parameter, though this could be simplified by assuming the same smoothing parameter across eigenfunctions through the prior $\psi_k \propto \exp \left\{ -\frac{h_\psi}{2\sigma^2} \psi_k^t \mathbf{P}_\alpha \psi_k \right\}$, where the smoothing parameter h_ψ does not depend on k .

We assume that the inverse variance components have the Gamma priors $1/\sigma^2 \sim \Gamma(\alpha_\sigma, \beta_\sigma)$, $1/\lambda_k \sim \Gamma(\alpha_\lambda, \beta_\lambda)$, and the smoothing parameters (which can be viewed as inverse of variance components) have Gamma priors $h_k \sim \Gamma(\alpha_\psi, \beta_\psi)$, for $k = 1, \dots, K$, and $h_\mu \sim \Gamma(\alpha_\mu, \beta_\mu)$. Here $\Gamma(a, b)$ denotes the Gamma distribution with mean a/b and variance a/b^2 . For details on specific choices of these priors, see the explicit STAN [31] implementation in Section 3. For a discussion on the choice of Gamma priors for inverse variance components, see, for example [7, 8].

Recall that the $Q \times K$ dimensional matrix Ψ has orthonormal columns if and only if the functions $\phi_k(\cdot)$ are orthonormal. The space of $Q \times K$ dimensional matrices with orthonormal columns is called the Stiefel manifold [19], which has a finite volume. We denote this space $\mathcal{V}_{Q,K}$ and assume a uniform prior on this space [23] proportional to $\mathbb{1}(\Psi \in \mathcal{V}_{Q,K})$. At the

data level, this induces a uniform prior on a particular linear subspace of $\mathcal{V}_{M,K}$ - the span of the spline basis functions. This span will include nearly all smooth functions for sufficiently large Q . We hypothesize that this works well in practice due to FPCA assuming smooth eigenfunctions, such that we reduce dimensionality without loss of viable eigenfunction forms. It is working with the much smaller $\mathcal{V}_{Q,K}$ Stiefel manifold of orthonormal spline basis coefficients, rather than the manifold $\mathcal{V}_{M,K}$ of eigenfunctions on the original space, which makes Fast BayesFPCA more efficient and stable.

2.3 Posterior and full conditionals

Given the conditional likelihood detailed in Section 2.1 and priors described in Section 2.2 the posterior likelihood $[\Theta|Y]$ of all model parameters, Θ , given the data, Y is proportional to

$$\begin{aligned} & \prod_{i=1}^N \prod_{m=1}^M N\{Y_i(t_m) | (Bw_\mu)_m + \sum_{k=1}^K \xi_{ik}(B\psi_k)_m, \sigma^2\} \times \Gamma^{-1}(\sigma^2 | \alpha_\sigma, \beta_\sigma) \\ & \times \left\{ \prod_{k=1}^K N(\xi_{ik} | 0, \lambda_k) \times \Gamma^{-1}(\lambda_k | \alpha_\lambda, \beta_\lambda) \times \exp\left(-\frac{h_k}{2\sigma^2} \psi_k^t \mathbf{P}_\alpha \psi_k\right) \times \Gamma(h_k | \alpha_\psi, \beta_\psi) \right\} \quad (2) \\ & \times \exp\left(-\frac{h_\mu}{2\sigma^2} w_\mu^t \mathbf{P}_\alpha w_\mu\right) \times \Gamma(h_\mu | \alpha_\mu, \beta_\mu) \times \mathbb{1}(\Psi \in \mathcal{V}_{Q,K}) \end{aligned}$$

Result 1. *The full conditionals of the scores, ξ_{ik} , and mean function parameters, w_μ , are normal. The full conditionals of the inverse eigenvalues, $1/\lambda_k$, inverse noise variance, $1/\sigma^2$, and the smoothing parameters h_μ , h_k for $k = 1, \dots, K$ have Gamma distributions. These distributions are provided in Supplement Section S2, with the exception of the full conditionals for the scores*

$$[\xi_{ik} | \text{others}] \sim N \left\{ \frac{\lambda_k (Y_i - \mathbf{B}w_\mu)^t \mathbf{B}\psi_k}{\lambda_k + \sigma^2}, \frac{\lambda_k \sigma^2}{\lambda_k + \sigma^2} \right\},$$

where $Y_i = \{Y_i(t_1), \dots, Y_i(t_M)\}^t$ is the $M \times 1$ dimensional vector of observations for study participant i .

Result 2. *The full conditional of the eigenfunction matrix Ψ has the generalized Bingham-Von Mises-Fisher (BMF) distribution*

$$[\Psi | \text{others}] \propto \exp \left[\text{tr} \left\{ -\frac{\Psi^t \mathbf{H} \Psi}{2\sigma^2} + \frac{\Xi^t (\mathbf{Y} - \mathbf{1}_N \otimes w_\mu^t \mathbf{B}^t) \mathbf{B} \Psi}{\sigma^2} \right\} \right] \mathbb{1}(\Psi \in \mathcal{V}_{Q,K}),$$

where $\mathbf{H} = \text{diag}(h_1, \dots, h_K)$, Ξ is a $N \times K$ dimensional matrix with the (i, k) entry equal to $\xi_{i,k}$, and the matrix \mathbf{Y} is the $N \times M$ dimensional matrix with the row i equal to Y_i^t . The quantity $\mathbf{1}_N$ is the N -dimensional column vector of ones, the symbol \otimes denotes the Kronecker product of matrices, and “tr” denotes the trace of a matrix.

2.4 The polar decomposition prior

The previous results indicate that all full conditionals are standard with the exception of the matrix Ψ . We will sample from this distribution indirectly by inducing a uniform prior on $\mathcal{V}_{Q,K}$. To that end, we introduce the polar decomposition of a $Q \times K$ matrix \mathbf{X} : $\mathbf{X} = \Psi\mathbf{P}$, where $\Psi \in \mathbb{R}^{Q \times K}$ is orthonormal and $\mathbf{P} \in \mathbb{R}^{K \times K}$ is positive semi-definite [5]. Here $\Psi = \mathbf{X}(\mathbf{X}^t\mathbf{X})^{-1/2}$ and $\mathbf{P} = (\mathbf{X}^t\mathbf{X})^{1/2}$ are standard formulae. Note that Ψ is on the Stiefel manifold by construction and is an explicit deterministic function of \mathbf{X} up to the matrix square root calculation algorithm. Crucially, if \mathbf{X} has independent $N(0, 1)$ entries, then Ψ is uniformly distributed on the Stiefel manifold [6]. Therefore, if we treat \mathbf{X} as the parameter in the model and we calculate Ψ , we sample from the posterior distribution described in Result 2. There are other techniques for implicitly placing distributions on the Stiefel manifold through alternative parameterization, particularly using Householder reflections or Givens Rotations, but we choose the Polar Decomposition for its implementation simplicity and comparatively similar computational efficiency [29, 21].

There are multiple ways to obtain the polar decomposition, but here we use the eigen-decomposition of $\mathbf{X}^t\mathbf{X} = \mathbf{Z}\mathbf{D}\mathbf{Z}^t$, defining $\Psi = \mathbf{X}\mathbf{Z}\mathbf{D}^{-1/2}\mathbf{Z}^t$ so that $\Psi^t\Psi = I_Q$, the identity matrix of dimension Q . There are important reasons why this decomposition works well in practice: (1) the uniform prior on Ψ can be induced indirectly via independent $N(0, 1)$ priors on the entries of \mathbf{X} ; (2) there is a deterministic relationship between \mathbf{X} and Ψ up to the choice of polar decomposition algorithm; (3) we work with the relatively small parameter matrix $\mathbf{X} \in \mathbb{R}^{Q \times K}$, as opposed to the matrix of eigenfunctions $\Phi \in \mathbb{R}^{M \times K}$ where $Q \ll M$; and (4) calculating Ψ from \mathbf{X} can be accomplished efficiently using linear algebra routines built into modern Bayesian software, such as STAN.

2.5 Extensions

Fast BayesFPCA can be easily extended to multilevel, structural, and longitudinal functional data analysis [11, 17, 30], structures that are increasingly common in applications. For example, functional observations from DASH4D have hierarchical structure - multiple meals observed for each participant. We demonstrate how to extend Fast BayesFPCA to fit a multilevel model. The data structure is of the form $Y_{ij}(t), i = 1, \dots, N, j = 1, \dots, J_i, t \in T = \{t_1, \dots, t_M\}$, where there are now J_i observations for each group i . In the DASH4D CGM example, I is the number of study participants, J_i is the number of meals for each study participant, and T is the number of measurements in the window around each meal. A first model for such data is the Gaussian MFPCA model [11, 38].

$$Y_{ij}(t) = \mu(t) + \eta_j(t) + \sum_{k=1}^{K_1} \xi_{ik}\phi_k^{(1)}(t) + \sum_{l=1}^{K_2} \zeta_{ijl}\phi_l^{(2)}(t) + \epsilon_{ij}(t). \quad (3)$$

where $\mu(t)$ is the population mean, $\eta_j(t)$ are visit-specific deviation from the population mean. The subject-level (level 1) deviations from the visit-specific mean are modeled by $U_i(t) = \sum_{k=1}^{K_1} \xi_{ik} \phi_k^{(1)}(t)$, where $\phi_k^{(1)}(t)$, $k = 1, \dots, K_1$ are the first level eigenfunctions, $\xi_{ik} \sim N(0, \lambda_k^{(1)})$, and $\lambda_k^{(1)}$ are the eigenvalues corresponding to $\phi_k^{(1)}(t)$. The subject/visit-specific (level 2) deviations from the subject-specific mean are modeled by $W_{ij}(t) = \sum_{l=1}^{K_2} \zeta_{ijl} \phi_l^{(2)}(t)$, where $\phi_l^{(2)}(t)$, $l = 1, \dots, K_2$ are the second level eigenfunctions, $\zeta_{ijl} \sim N(0, \lambda_l^{(2)})$, and $\lambda_l^{(2)}$ are the eigenvalues corresponding to $\phi_l^{(2)}(t)$. Finally, $\epsilon_{ij}(t) \sim N(0, \sigma^2)$ is the error process. All functional components, $\epsilon_{ij}(t)$, $U_i(t)$ and $W_{ij}(t)$, are assumed to be mutually uncorrelated.

The population mean $\mu(t)$ and the visit-specific deviations $\eta_j(t)$ are modeled using penalized spline expansion in the same fashion Fast BayesFPCA models $\mu(t)$. Inspection of $U_i(t) = \sum_{k=1}^{K_1} \xi_{ik} \phi_k^{(1)}(t)$ shows it is the same component in (1), so we can use the approach described in Sections 2.2, 2.3, and 2.4. The only new component, $W_{ij}(t) = \sum_{l=1}^{K_2} \zeta_{ijl} \phi_l^{(2)}(t)$, can be treated the same as $U_i(t)$, modeling the eigenfunctions using spline expansion with an independent polar decomposition prior on the level 2 coefficient matrix.

A completely Bayesian approach to multilevel FPCA which explicitly models the eigenfunctions has not been implemented in the literature. The code for this multilevel extension is presented in the code repository linked in Supplement Section S3.1.

3 Bayesian implementation in STAN

The methods described in Section 2 need to be implemented and tested in simulations and applications. This is facilitated when the software is simple, scalable, and adaptable to changes in the specific models and data structures. In this section we provide the STAN [31] implementation of Fast BayesFPCA.

This `data` section is self-explanatory, declaring constants and importing the data, spline basis, and penalty matrix. All notation is as used in the text.

```
// Provide the data sources
data{
  int N; // Number of time series
  int M; // Number of observations
  int Q; // Number of spline bases
  int K; // Number of Eigenfunctions

  matrix[N, M] Y; // Functional data
  matrix[M, Q] B; // Orthogonal spline basis
  matrix[Q, Q] P; // Penalty matrix for splines
}
```

In the `parameters` block, we notably treat \mathbf{X} (\mathbf{X}) as a parameter rather than Ψ , which

we instead obtain from \mathbf{X} . This is an essential part of Fast BayesFPCA. This block also contains the eigenvalues λ_k (`lambda`) stored in a `positive_ordered` type. Within STAN, this variable type enforces ascending ordering, facilitating soft-ordering of the eigenvalues and corresponding eigenfunctions. The matrix `Scores` is the $N \times K$ dimensional score matrix Ξ introduced in Result 2. The (i, k) entry of this matrix is equal to ξ_{ik} .

```
// Declare the parameters
parameters{
  real<lower=0> sigma2; // Error in observation

  // Mean structure
  vector[Q] w_mu; // Population mean parameters
  real<lower=0> h_mu; // Population mean smoothing parameter

  // Covariance structure
  positive_ordered[K] lambda; // Eigenvalues
  vector<lower=0>[K] H; // EF smoothing parameters
  matrix[Q, K] X; // Unconstrained EF weights (X)
  matrix[N, K] Scores; // EF scores (xi)
}
```

The `transformed parameters` section contains important quantities derived from deterministic functions of the data and sampled model parameters. The key component of this block is the definition of the Ψ matrix (`Psi`). We use the definition of the Polar Decomposition to define $\Psi = \mathbf{XZD}^{-1/2}\mathbf{Z}^t$, where \mathbf{Z} (`evect_XtX`) is the $K \times K$ dimensional matrix of eigenvectors of $\mathbf{X}^t\mathbf{X}$ and \mathbf{D} (`diag(eval_XtX)`) is a diagonal matrix containing the corresponding K eigenvalues. We compute these components using the linear algebra library underlying STAN. We use `Psi` in the model likelihood, but induce the prior on this matrix through `X`.

```

// Calculate observed parameters from latent
transformed parameters{
  // Population mean
  vector[M] mu = B * w_mu;

  // Eigenvalues
  vector[K] eval = reverse(lambda);

  // Orthonormal EF weights
  matrix[Q,K] Psi;

  // Polar decomposition
  {
    matrix[K,K] evec_XtX = eigenvectors_sym(X'*X);
    vector[K] eval_XtX = eigenvalues_sym(X'*X);
    Psi = X*evec_XtX*diag_matrix(1/sqrt(eval_XtX))*evec_XtX';
  }
}

```

The model proceeds with the specification of priors within the `model` section. The smoothing parameters h_μ (`h_mu`) and h_k , $k = 1, \dots, K$ (`H`) are assigned independent Gamma priors. The eigenvalues λ_k , $k = 1, \dots, K$ and the error variance σ^2 (`sigma2`) have independent inverse Gamma priors. Smoothing priors on the population mean, $\mu(t)$, and eigenfunctions, $\phi_k(t)$, are implemented via quadratic penalties on their coefficients; see Section 2.2 for more details. Note that Fast BayesFPCA's `STAN` implementation does not require the penalty matrix \mathbf{P}_α within these quadratic penalty terms to be full rank.

The next step is inducing the prior on Ψ , which just requires specifying independent $N(0, 1)$ priors for each entry of the matrix \mathbf{X} (`X`). This is efficiently accomplished with vectorization. Combined with the definition of Ψ in the `transformed parameters` block, this induces a uniform prior on Ψ over the Stiefel manifold. This means we model the small-dimensional $Q \times K$ matrix \mathbf{X} , constrained by the size of the spline basis and number of eigenfunctions. We can efficiently polar decompose this small matrix to get Ψ , an important point as this is repeated at every step of the posterior simulation. Moreover, the matrix Ψ is much lower dimensional ($Q \times K$) compared to the $M \times K$ dimensional matrix used by [20]. These advantages translate into more stable and faster inference compared to the current state-of-the-art and will allow generalization to more complex models.

We next pre-compute each $\theta_i(t) = \sum_{k=1}^K \xi_{ik} \phi_k(t)$, which is equal to $\sum_{k=1}^K \xi_{ik} \{ \sum_{q=1}^Q B_q(t) \psi_{qk} \}$, where ψ_{qk} is the q th entry of the $Q \times 1$ dimensional vector ψ_k . If Θ is the $N \times M$ dimensional matrix with (i, m) entry equal to $\theta_i(t_m)$, it can be shown that $\Theta = \Xi \Psi^t \mathbf{B}^t$. We denote Θ as `Theta`. This value is computed once for each sample and not saved to conserve memory.

The data likelihood is finally expressed in terms of $M \times 1$ dimensional vectors of observations $\mathbf{Y}_i = \{Y_i(t_1), \dots, Y_i(t_m)\}^t$ for all study participants i . The Bayesian FPCA model assumes that

$$Y_i(t_m) \sim N\{\mu(t_m) + \theta_i(t_m), \sigma^2\},$$

where recall that $\theta_i(t_m) = \sum_{k=1}^K \xi_{ik} \{\sum_{q=1}^Q B_q(t_m) \psi_{qk}\}$.

```
// Specify likelihood and priors
model{
  // Smoothing parameter priors
  H ~ gamma(1, 0.005);
  h_mu ~ gamma(1, 0.005);

  // Eigenvalue priors
  lambda ~ inv_gamma(0.1,0.001);

  // Error variance prior
  sigma2 ~ inv_gamma(1,0.001);

  // Smoothing additions to the target density
  target += -(1 * h_mu)/(2 * sigma2) * w_mu' * P * w_mu;

  for(i in 1:K){
    target += -(1 * H[i])/(2 * sigma2) * Psi[,i]' * P * Psi[,i];
  }

  // Indirect uniform prior on Stiefel manifold
  to_vector(X) ~ normal(0,1);

  // FPCA-based Score priors
  for(i in 1:K){
    to_vector(Scores[,i]) ~ normal(0, sqrt(eval[i]));
  }

  // Data Likelihood
  {
    matrix[N,M] Theta = Scores * (B * Psi)'; // Calculate linear predictors
    for(i in 1:N){
      Y[i,] ~ normal(mu + to_vector(Theta[i,]), sqrt(sigma2));
    }
  }
}
```

We present the simplest possible Bayesian FPCA analysis, though this implementation extends easily to other examples. For a multilevel FPCA, we need to construct Ψ_1 and Ψ_2 (instead of just Ψ). We use the same approach and consider now two smaller-dimensional latent matrices \mathbf{X}_1 and \mathbf{X}_2 . We assume that each of their entries has an independent $N(0, 1)$ prior. The Ψ_1 and Ψ_2 matrices are obtained via polar decompositions in the `transformed parameters` section using the same approach described above for the single level Bayesian FPCA. All other components of the model implementation are relatively standard and just require careful accounting of indices. We present both the implementation and simulation evaluation of this approach in the supplementary materials.

4 Simulations

We consider two simulation scenarios for model (1), adopting $t \in [0, 1]$ for simplicity. We use $f_k(\cdot)$ for the Legendre polynomial of order k rescaled to the domain $[0, 1]$ [34]. We leverage the orthogonality of both the Legendre and Fourier bases in constructing the simulation eigenfunctions. We append scaling constants to ensure the discretely observed eigenfunctions have norm 1.

Scenario 1. (S1)

$$\begin{aligned}\phi_k(t) &= \left\{ \frac{1}{\sqrt{M}} f_0(t), \sqrt{\frac{84}{31M}} [f_1(t) - 0.5f_3(t)], -\sqrt{\frac{5}{M}} f_2(t) \right\}; \\ \lambda_k &= \{45000, 7000, 2000\}; \quad \sigma^2 = 4; \quad \mu(t) = 140 - 10f_2(t)\end{aligned}$$

Scenario 2. (S2)

$$\begin{aligned}\phi_k(t) &= \left\{ \sqrt{\frac{1}{3M}} [1 - 2 \cos(2\pi t)], \sqrt{\frac{1}{15M}} [5 \sin(2\pi t) - \sin(4\pi t) - 2 \cos(2\pi t)] \right\} \\ \lambda_k &= \{25000, 8500\}; \quad \sigma^2 = 121; \quad \mu(t) = 10 - 5 \sin(2\pi t) - 5 \cos(2\pi t)\end{aligned}$$

Both simulation scenarios are obtained from analyses of real datasets: S1 is meant to replicate the aggregated CGM data Section 5, while S2 is based on physical activity data from wrist-worn accelerometry in NHANES [9]. The second data set is not analyzed in this paper, but provides a realistic simulation scenario using publicly available data. A comparison of these model components and their corresponding estimates from the DASH4D and NHANES data, respectively, is presented in Supplemental Figure S1. All code for performing simulations is publicly available through GitHub; link provided in the online supplement.

For each scenario we generate 100 datasets with $N = 50$ functions observed at $M = 30$ equally spaced points within $[0, 1]$. Fast BayesFPCA ("FAST") is compared to the

Generalized Function-on-Scalar Regression of Goldsmith et al., 2015 [16] (labeled "GFSR") and the polar expansion in the observed data space [20] (labeled "SVD-GP" for the SVD data structure with centered Gaussian Process prior on the eigenfunctions). We do not compare with [37] nor [24], as they provide no software and no means of performing inference on the functional components respectively.

The SVD-GP method does not include a general mean $\mu(t)$ as published. We extend the model to include this component, sampling $\mu(t)$ as an observation of an underlying Gaussian Process with a smoothing covariance prior similar to that of the $\phi_k(t)$. We extract the corresponding scores directly, regardless of the model's additional constraint of score matrix orthonormality.

While the FAST and SVD-GP models explicitly sample all FPCA model components, GFSR instead samples the smooth functions $\hat{\mu}(t)$ and $\hat{\theta}_i(t) = \sum_{k=1}^K \hat{\xi}_{ik} \hat{\phi}_k(t)$. To retrieve the corresponding eigenfunctions, we must apply SVD to the $\hat{\theta}_i(t)$ samples, taking the right singular vectors. We then use GAM to project $Y_i(t) - \hat{\mu}(t)$ onto the eigenfunctions for each sample to get the corresponding scores.

For all three methods, we aligned the eigenfunctions and derived eigenfunction estimates from the posterior samples. With the former, we address potential sign flipping due to the inherent non-identifiability of eigenfunction and score signs in FPCA. We align eigenfunctions and corresponding scores to maximize correlation with the first posterior sample. We can then further align the posteriors with the ground truth using the same method. As eigenfunctions exist generally in $\mathbb{R}^{M \times K}$, we require a concept of posterior "mean" which maintains orthonormality. We derive posterior eigenfunction estimates for FAST and SVD-GP by taking the pointwise Euclidean mean of the eigenfunction samples and projecting the result onto the corresponding Stiefel Manifold. GFSR on the other hand takes the right singular vectors from the SVD of the mean smooth matrix, as is recommended by the authors [16].

We first focus on the Integrated Square Error for the mean, $\mu(t)$ and principal components $\phi_k(t)$, evaluated at the time points t_m , $m = 1, \dots, M$. For example, if $\hat{\mu}^b(t)$ is the posterior mean of $\mu(t)$ conditional on the simulated data set $b = 1, \dots, B$, the Integrated Square Error (ISE) is defined as:

$$\text{ISE}^b\{\mu(\cdot)\} = \frac{1}{M} \sum_{m=1}^M \{\hat{\mu}^b(t_m) - \mu(t_m)\}^2.$$

Combining these values over simulations provide a B -dimensional vector for each method. Similar definitions apply to principal components.

Figure 1 displays the boxplots of the ISE distributions for the mean (first panel column) and principal components (second to fourth panel columns) for scenario S1 (first row of panels) and scenario S2 (second row of panels). Boxplots are shown for FAST in red, for GFSR in green, and for SVD-GP in blue. The y-axis in every plot is on the log

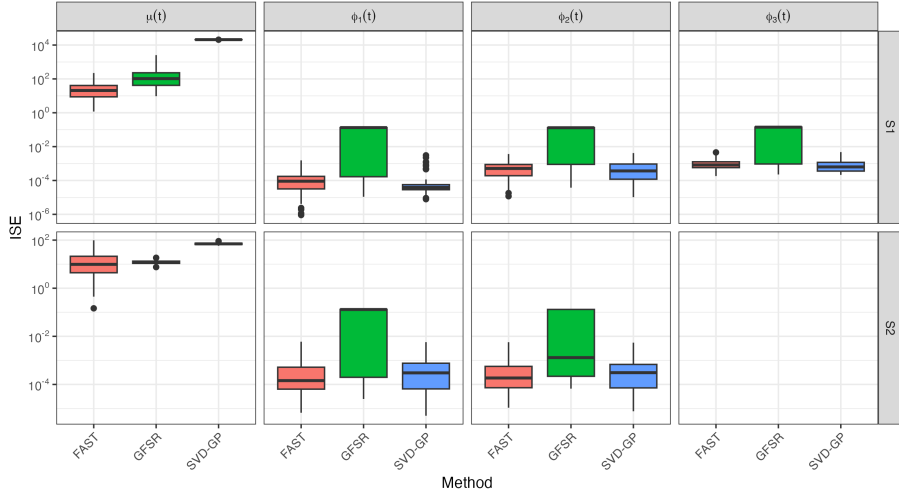


Figure 1: Boxplots of the ISE for the mean and eigenfunctions for FAST (red), GFSR (green), and SVD-GP (blue). First row: S1; second row: S2. Each column: mean or corresponding eigenfunction. Y-axis is on the log scale for presentation purposes. Results shown for $N = 50$ functions with $M = 30$ observations per function.

scale for presentation purposes, as the eigenfunctions are on a different scale from the mean function. FAST has ISE which is either comparable or superior to the other two methods for all functional components, with eigenfunction MSE for GFSR appearing to be particularly poor. It is not entirely clear why this occurs, though we speculate that GFSR can encounter identifiability issues when estimating a combined set of fixed effects (mean) and random effects (covariance) with similar structure. To mitigate this, FAST begins sampling in the neighborhood of reasonable $\mu(t)$ and λ_i estimates.

We have also calculated the posterior coverage probabilities for the true mean $\mu(t)$ and eigenfunctions $\phi_k(t)$, $k = 1, \dots, K$. For each simulated data set $b = 1, \dots, B$, we obtain the equal-tail 95% credible intervals at all time points t_m , $m = 1, \dots, M$ along the domain of the functions. The proportion of times these credible intervals cover the true function is calculated over t_m for each combination b, k . These proportions are then collected in a vector of $B = 100$ proportions for each function $\phi_k(t)$, respectively. Figure 2 displays the kernel smooth of these vectors of proportions for the mean and eigenfunction estimates produced by FPCA (red), GFSR (green), and SVD-GP (blue). The first row of panels corresponds to S1, and the second presents results from S2. FAST has superior, or closer to nominal, coverage probabilities to both GFSR and SVD-GP for these functions.

For each simulated data set $b = 1, \dots, B = 100$, each subject $i = 1, \dots, I = 50$, and each FPC $\phi_k(t)$, $k = 1, \dots, K$, there is a simulated true score, $\xi_{ik}^b \sim N(0, \lambda_k)$. Each combination of dataset b and FPC k thus has $I = 50$ scores ξ_{ik}^b . For each such combination b, k , we calculate the proportion of times the equal-tail 95% credible intervals cover the corresponding true scores. These proportions are collected in a vector of $B = 100$ proportions

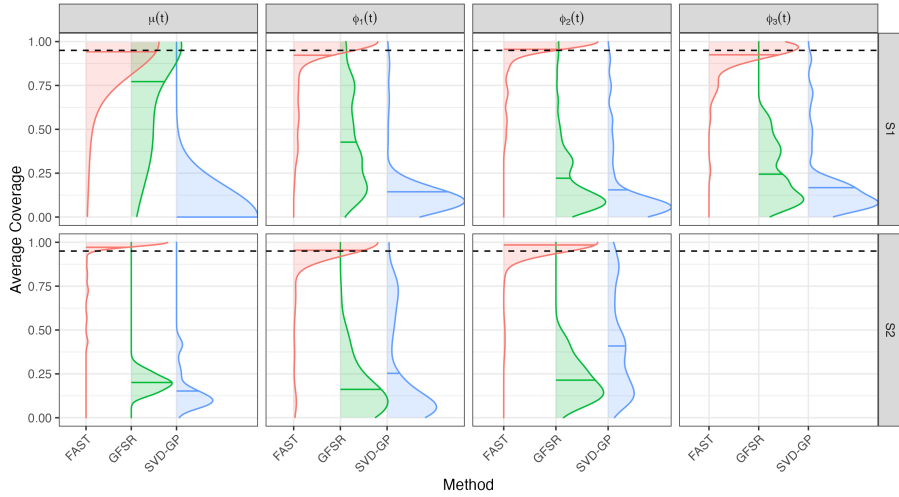


Figure 2: Kernel smoother of coverage probabilities of 95% credible intervals of the true mean and eigenfunctions for FPCA (red), GFSR (green), and SVD-GP (blue). First row: S1; second row: S2. Each column: corresponding function. Distribution means: horizontal solid lines; nominal 95% level: horizontal dotted lines. Results shown for $N = 50$ functions with $M = 30$ observations per function.

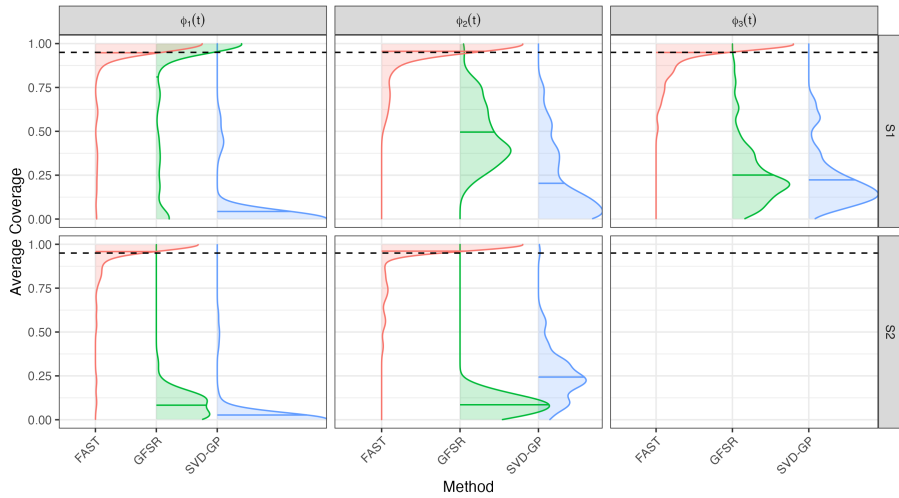


Figure 3: Kernel smoother of coverage probabilities of 95% credible intervals of the true scores, ξ_{ik}^b , for FAST (red), GFSR (green), and SVD-GP (blue). First row: S1; second row: S2. Each column: corresponding eigenfunction. Distribution means: horizontal solid lines; nominal 95% level: horizontal dotted lines. Results shown for $N = 50$ functions with $M = 30$ observations per function.

for each FPC. Figure 3 displays the kernel smooth of these vectors of proportions for FAST (red), GFSR (green), and SVD-GP (blue) by eigenfunction in Scenario S1 (first row) and Scenario S2 (second row). FAST achieves nearly nominal coverage for all FPCs in both

scenarios, while GFSR and SVD-GP are not close.

It is unclear exactly why the GFSR and SVD-GP methods do not perform well in terms of coverage probabilities for the scores and eigenfunctions. For the GFSR method, the poor coverage could be due to not accounting for the uncertainty in the Kosambi-Karhunen-Loève (KKL) decomposition. One possibility for the SVD-GP could be that this method introduces substantial bias by enforcing orthogonality between eigenfunction scores.

We extended the above simulations both to a larger observation grid $M = 60$ and to a multilevel scenario, detailed in Supplemental material Sections S3.2 and S3.3 respectively. It is important to note here that the GFSR method is the only one which actually has a multilevel implementation at this time, so it is the only comparator for this new scenario. In the case of both extensions, we find qualitatively similar comparisons of performance to those detailed here.

We compare the S1 and S2 computation times for the three methods when $N = 50$, $M \in \{30, 60\}$ in Supplemental Table S1. To quickly summarize, FAST is more computationally efficient, by a factor of 2-4 times, than both the GFSR and SVD-GP methods in every scenario. This advantage becomes more pronounced as M and N scale. Table 1 contains the computation times from a personal laptop for all three methods with $N = 50$ and M becoming large (left column), as well as with $M = 30$ and N becoming large. This Table indicates that computation time and resource use for SVD-GP scale poorly with the number of observations M along the functional domain, with a similar pattern observed for GFSR when the number of time series N increases. At the largest tested values ($M = 1000$ and $N = 1000$), we were unable to complete fitting SVD-GP and GFSR at all due to memory usage and unreasonable compute time, respectively. In contrast, FAST scales nearly linearly with both N and M , such that we can fit models with large N and M using this procedure. To gain a better sense of this difference, we visualize these scaling behaviors up to $M = 300$, $N = 300$ in supplemental Figures S8 and S9 respectively. These outcomes agree with complexity analysis of the linear algebra and other operations performed outside of MCMC sampling. Operations in FAST are at most linear in both N and M , while SVD-GP scales as $O(M^3)$ due to Polar decomposing at the data level and GFSR scales as $O(N^3)$ due to using GAM in post-processing to calculate the scores [36].

5 Data analysis

5.1 The DASH4D CGM Study

Dietary Approaches to Stop Hypertension for Diabetes (DASH4D, NCT04286555) is a nutritional trial designed to assess how blood pressure and glucose respond to combinations of DASH-style and low-sodium diets in persons with type 2 diabetes (T2D). The study team

Fixed $N = 50$				Fixed $M = 30$			
Times (min)				Times (min)			
M	FAST	GFRS	SVD-GP	N	FAST	GFRS	SVD-GP
30	1.1	4.4	1.9	50	1.0	4.1	2.5
100	1.9	8.0	11.2	100	1.7	13.4	2.9
300	4.3	15.4	124.6	300	5.4	130.6	5.8
1000	18.0	64.6	—	1000	18.2	—	27.8

Table 1: Table of observed computational times for each combination of scenario and method. Simulation S1 is used in all cases. SVD-GP was not able to complete estimation for $N = 50, M = 1000$ due to excessive RAM usage ($>16\text{GB}$), and GFRS was stopped prematurely for $N = 1000, M = 30$ due to taking an unreasonably long time (>2 days).

prepared four diets: DASH4D diet with lower sodium, DASH4D diet with higher sodium, Comparison diet with lower sodium, and Comparison diet with higher sodium. Weight was held constant by adjusting calorie levels, if needed. Effects of these diets were observed through a single-site, 4-period crossover design [1]. Each period consisted of 5 weeks of feeding one of the diets followed by at least a 1-week break (median 2 weeks). There were $N = 105$ randomized T2D participants recruited from the Baltimore area, of which the $N = 65$ with meal timing data were a subset. The participants with meal timing data had a median age of 68 years, were 66% female, and had the following race distribution: 6.2% Asian, 87.7% Black, and 6.2% White.

Within the context of DASH4D, the DASH4D CGM study was conducted to evaluate impact of the dietary intervention on glucose assessed by CGM. Participants wore Abbott Freestyle Libre Pro sensors (Abbott Diabetes Care), placed near the middle of the third week and worn into the fifth week for each observation period. The CGM devices were placed on the back of the upper arm (approved location) by trained technicians [12]. These devices record interstitial glucose every 15 minutes. The Libre Pro is a masked CGM system, so participants were not aware of the glucose measurements.

5.2 Mealtime CGM glucose

During feeding periods, including CGM wear, participants ate meals at the study site 3 days each week. Clinic staff observed consenting participants during these meals to document the time of meal initiation. We used these timestamps to align the CGM data into 5 hour periods starting 1 hour before and ending 4 hours after meal initiation. For each study participant, there were up to 20 such five-hour periods. The final dataset comprised 768 meals over 65 participants.

Figure 4 provides a visualization of mealtime CGM for four randomly-sampled study

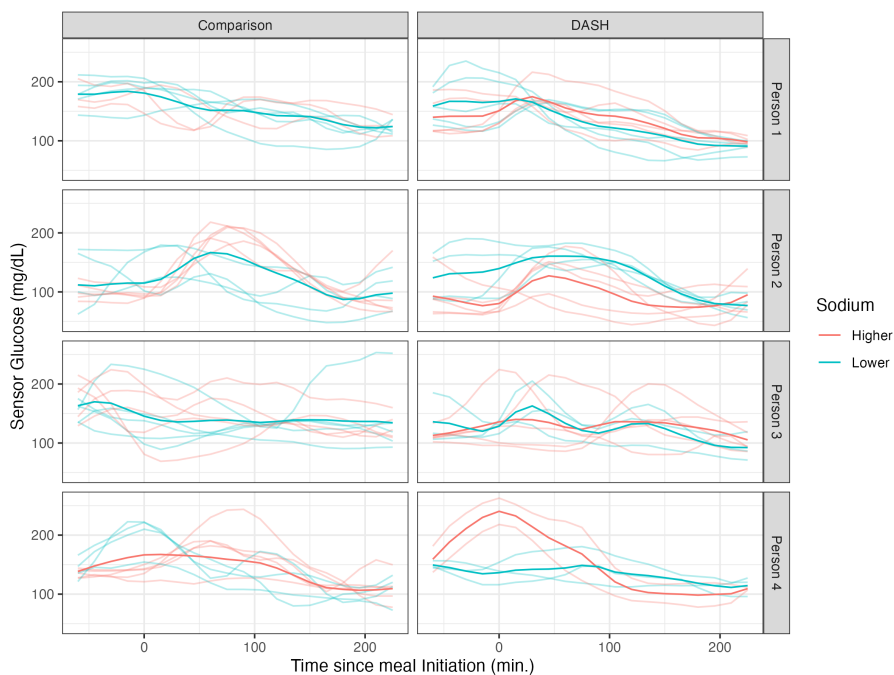


Figure 4: Mealtime CGM for 4 participants (one participant per row), for the DASH (left panels), Comparison (right panels) diets, lower sodium (blue curves), and higher sodium (red curves) diets. X-axis: time from meal initiation, y-axis: CGM in mg/dL. Person- and diet-specific averages are shown as darker curves, while meal-specific mealtime curves are lighter curves.

participants. The x-axis in each panel corresponds to time in minutes from meal initiation; the y-axis is the recorded interstitial glucose. Each row of two panels reports the CGM curves for one participant. The first column is for Comparison meals, and the second is for DASH meals. The curve color corresponds to lower or higher sodium diets. The darker curves are the within-person average curves.

The data structures in Figure 4 suggest applying either Bayesian FPCA to the participant average curves or using a two-level Bayesian FPCA to capture both the participant-specific averages (level 1) and the meal-specific deviations (level 2) within each diet. We undertake both analyses in Sections 5.3 and 5.4 respectively.

5.3 Bayesian FPCA of average CGM within diets

We fit Fast BayesFPCA on the participant-specific CGM curves for each diet separately (darker curves in Figure 4) and compared results across diets. We use spline basis of dimension $Q = 10$ for $K = 3$ eigenfunctions. As the number of curves per-diet ranges from 36 to 49, accounting for variability in FPCA component estimates is of particular importance [15].

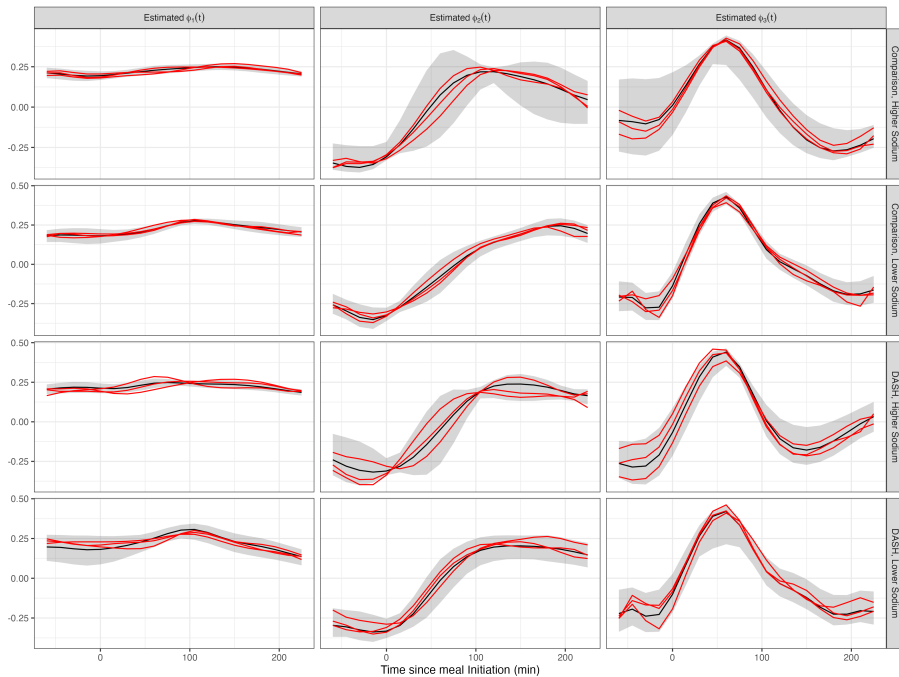


Figure 5: Bayesian FPCA results for the first three PCs (each column corresponds to one FPC) for each of the four diets (each row corresponds to one diet). X-axis: time from the start of the meal. Black curves: posterior mean; red curves: three samples from the posterior of the PCs; shaded areas: pointwise 95% credible intervals.

Figure 5 displays results for Bayesian FPCA inference for the first three PCs (each column corresponds to one FPC) for each of the four diets (each row corresponds to one diet). For each panel the x-axis is the time from the start of the meal, the black curves are the posterior means, the red curves are three samples from the posterior of the PCs, and the shaded areas are point-wise, equal-tail 95% credible intervals. We visualize the posterior samples to better demonstrate joint sampling variability in the set of eigenfunctions. Each set of red FPC curves corresponding to the same iteration is a posterior realization on the Stiefel manifold.

Figure 6 visualizes how the mealtime glucose variability decomposes among the eigenfunctions of Figure 5. The left panel indicates the mean and equal-tail 95% credible interval of eigenvalues associated with each FPC and diet, while the right provides the corresponding percent variability quantities. Each diet is shown using a distinct color.

Posterior eigenfunction estimates $\hat{\phi}_k(t)$ are qualitatively similar across diets in Figure 5. The primary modes of variability $\hat{\phi}_1(t)$ are all nearly constant with a small curvature. Higher scores on these components correspond to higher CGM responses over the entire mealtime period. The sample-to-sample variability in the shape of $\phi_1(t)$ is relatively low across diets, indicating high confidence in the posterior mean curves. As indicated by Figure 6, $\hat{\phi}_1(t)$ explains the majority of observed variability, regardless of diet. This reinforces

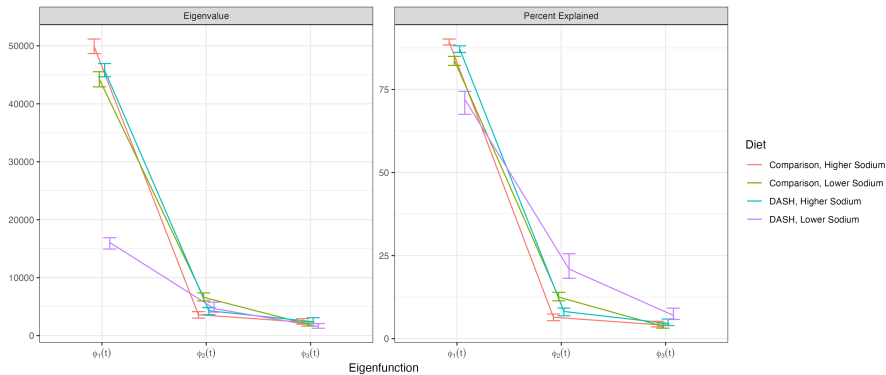


Figure 6: Eigenvalue and percent-variability estimates from the Bayesian FPCA models fit to each of the four diets (each line and color corresponds to one diet). X-axis: eigenfunction corresponding to eigenvalue/percent variance explained. All estimates are presented with their corresponding 95% credible intervals.

existing literature on the importance of average postprandial glucose levels [14].

We consider the $\hat{\phi}_2(t)$ and $\hat{\phi}_3(t)$ together, as they explain relatively little of the observed variability according to eigenvalues. The second most prominent modes $\hat{\phi}_2(t)$ generally have an S pattern, such that larger scores correspond to lower glucose in the pre-prandial hour, increase over the hour post-meal, and a larger response two to four hours after eating. The estimates $\hat{\phi}_3(t)$ are all negative during the hour before the meal, increase quickly to a peak positive value around 50 to 70 minutes after food intake, and decrease relatively quickly back to negative values around minutes 150 – 200. Higher scores on $\hat{\phi}_3(t)$ correspond to below-average fasting glucose and rapid uptake after the meal. The sample-to-sample variability of $\phi_2(t)$ and $\phi_3(t)$ are much higher than that of $\phi_1(t)$. These variations could be due to the lack of separation of the eigenvalues; for further discussion, see [13].

Turning to Figure 6, we find that the variability decomposes uniquely for the DASH/lower sodium diet. This diet exhibits lower variability according to eigenvalue sum, driven by a much smaller eigenvalue associated with $\hat{\phi}_1(t)$. This diet, of primary interest to the DASH4D study, thus appears to have lower inter-participant variability in mean glucose level. While this finding requires further validation, it could indicate more stable glycemic response among poorly controlled individuals while on this diet. Other features of variability decomposition are qualitatively similar between diets.

Fast BayesFPCA fit stably and produced reasonable results, qualitatively similar to standard FPCA, across all four diets. Though, Fast BayesFPCA provides unique uncertainty quantification of functional estimates. Moreover, each model took just over a minute to fit on a standard laptop using 4500 warm-up samples and 500 posterior samples.

We recognize that the mean CGM curves are derived from differing numbers of functional observations within each participant/diet combination, so they will vary in obser-

vation noise. We can instead randomly select single curves from each such combination to more appropriately model the person-specific processes (completed in Supplement Section S4 to qualitatively similar results), but this is infrequently done by practitioners due to the data waste. To both appropriately model all sources of variability within each diet and use all data, we turn to a flexible multilevel modeling structure.

5.4 Bayesian MFPCA of individual CGM curves

We fit the multilevel extension of Fast BayesFPCA described in Section 2.5 for each diet separately, where the first level corresponds to the study participant and the second level corresponds to the meal. We use spline basis dimension $Q = 10$, $K_1 = 2$ eigenfunctions at the subject level, and $K_2 = 3$ eigenfunctions at the meal level. The number of observed meals ranges from 147 to 219 for each diet, with at most five meals for each combination of participant and diet. The main goal of the analysis is to characterize mealtime CGM variability within each diet at the person and meal levels [16]. As there is no reason to assume that meal/visit order has effect, for this analysis we set $\eta_j(t) = 0$ for all j .

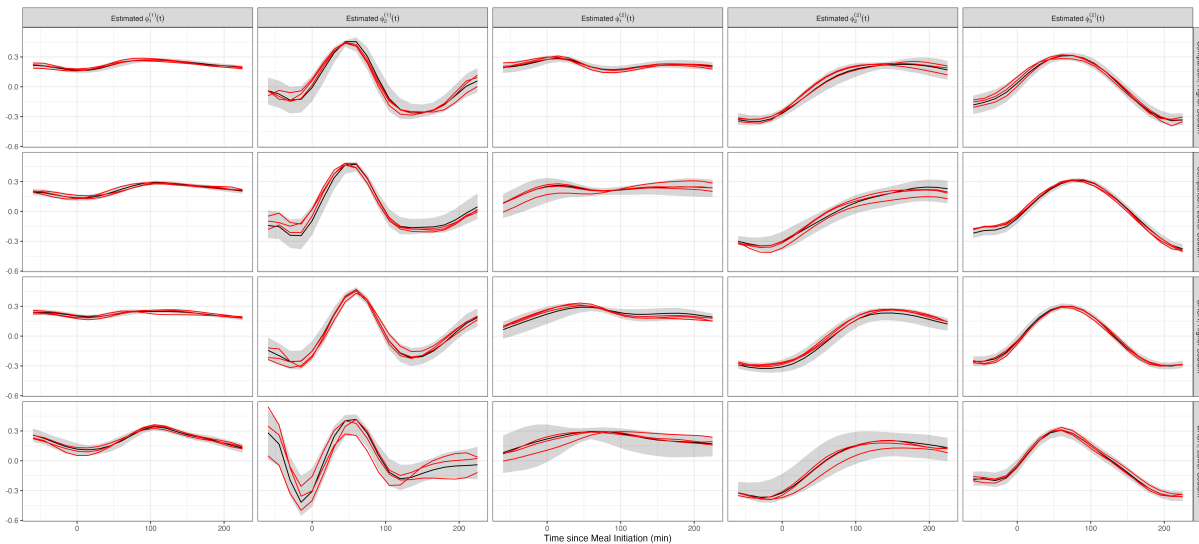


Figure 7: Bayesian MFPCA results for the first two PCs at the subject level and first three PCs at the meal level. Each column corresponds to one FPC and each row corresponds to a diet. X-axis: time from the start of the meal. Black curves: posterior mean; red curves: three samples from the posterior of the PCs; shaded areas: pointwise 95% credible intervals.

Figure 7 displays the Bayesian MFPCA results, with row indicating diet and column indicating FPC. The first two columns correspond to the subject level, while the last three column correspond to the meal level. For each panel the x-axis is the time from the start of the meal, the black curves are the posterior means, the red curves are three samples from

the posterior of the PCs, and the shaded areas are pointwise 95% credible intervals. Each set of red FPC curves corresponding to the same iteration is a posterior realization on the subject- and meal-level Stiefel manifolds.

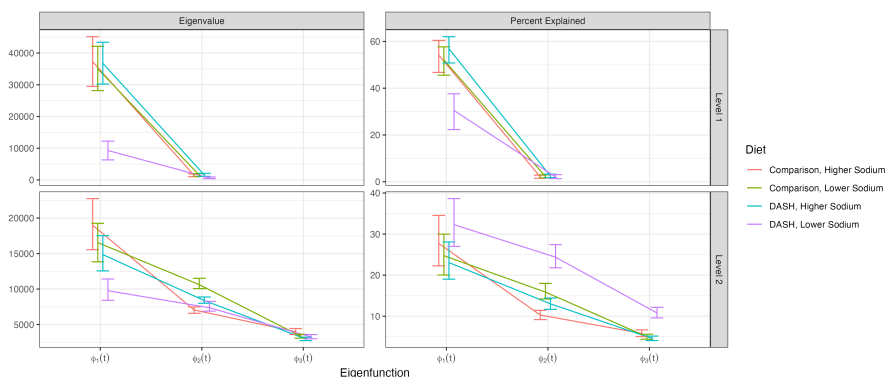


Figure 8: Eigenvalue and percent-variability estimates from the Bayesian MFPCA models fit to each of the four diets (each color corresponds to one diet). X-axis: eigenfunction corresponding to eigenvalue/percent variance explained. All estimates are presented with their corresponding 95% credible intervals.

Figure 8 illustrates the estimated variability decomposition both by eigenfunction and hierarchical level within each diet. The left column of panels indicate the mean and 95% equal-tail credible intervals for the eigenvalues associated with each eigenfunction, while the right provides the corresponding percent variability quantities. The rows correspond to level of the hierarchy, with the first being subject (Level 1) and second being meal (Level 2). Each diet is shown using a distinct color.

Similar to the FPCA case, Figure 7 indicates mostly qualitative similarity of estimates $\widehat{\phi}_k^{(1)}(t), \widehat{\phi}_l^{(2)}(t)$ across diets. The primary mode of variability within each diet is $\widehat{\phi}_1^{(1)}(t)$, a nearly constant function. Higher subject scores on this component correspond to higher glucose over the entire observation window. The sample-to-sample variability in shape of $\phi_1^{(1)}(t)$ is low within all diets, indicating high confidence in this functional form. There is some heterogeneity in the percent variability explained by this component, but it is $\geq 35\%$ in every case.

The next most important eigenfunction, according to eigenvalue, is uniformly $\widehat{\phi}_1^{(2)}(t)$. This eigenfunction is also nearly constant and has low sampling variability, though there appears to be a small positive slope prior to meal initiation for all but the Comparison, Higher Sodium diet. This suggests that these intervention diets could be associated with lower fasting CGM measurements. These secondary modes of variability explain between 23 – 33% of total variability according to Figure 8. Taken with the functional form of $\widehat{\phi}_1^{(1)}(t)$, we observe that mean glucose level is the main source of variability in mealtime CGM curves.

Among all diets, $\widehat{\phi}_2^{(2)}(t)$ at the meal level is the third most prominent mode of variability (10 – 25% explained), taking an S pattern. As in the single-level case, larger scores correspond to lower glucose in the pre-prandial hour, increase over the hour post-meal, and a larger response two to four hours after eating. The final eigenfunctions $\widehat{\phi}_2^{(1)}(t)$, $\widehat{\phi}_3^{(2)}(t)$ capture higher-order glyceimic reaction patterns and explain much smaller proportions of variability (< 12% explained).

The variability partitioning within- and between-study participants presented in Figure 8 indicates a unique decomposition for the DASH/Lower Sodium diet, as in the single-level analysis. First, this diet has substantially lower overall variability, as indicated by sum of eigenvalues. Second, this difference is again driven by the variability associated with the mean level mode(s), $\widehat{\phi}_1^{(1)}(t)$ and $\widehat{\phi}_1^{(2)}(t)$. The equal-tail credible intervals for the associated eigenvalues are mutually exclusive to those of the other diets, with a particularly large absolute difference at the subject level. This potentially indicates that indeed there is a blunting of person-specific glyceimic response for more extreme individuals, though further analysis is still required for verification. Finally, there appears to be greater relative within-participant variability for the DASH/Lower Sodium diet, with the eigenfunctions $\phi_l^{(2)}(t)$ having greater estimates of variability explained than the corresponding functions in the comparator diets. This is potentially a result of both the reduced mean CGM variability as well as the greater nutritional variety present in this healthier diet, but further examination is required to be sure.

Each Bayesian MFPCA model takes ≈ 15 minutes to run on a standard laptop with 4500 warm-up samples and 500 samples from the posterior. We use this large number of warm-up samples out of an abundance of caution. Simulations indicate that as little as 1000 warm-up samples could be used. The posterior sampling is stable and had no major issues.

5.5 Model Checking

Model diagnostics were conducted to study the stability of MCMC sampling. We generate trace plots of eigenfunctions evaluated at particular points along the temporal domain: $t = -45, 75$, and 210 minutes relative to meal initialization. These trace plots, found in Supplement Sections S5 and S6 respectively, display posterior samples from 4 chains in different colors. For all eigenfunctions from both FPCA and MFPCA, the trace plots demonstrate good mixing and minimal autocorrelation.

To investigate whether our FPCA and MFPCA models fit the data well, we compared posterior samples of underlying smooths to the raw data. These smooths are calculated as $\widehat{Y}_i(t) = \widehat{\mu}(t) + \sum_{k=1}^K \widehat{\xi}_{ik} \widehat{\phi}_k(t)$ for the FPCA models and $\widehat{Y}_{ij}(t) = \widehat{\mu}(t) + \sum_{k=1}^{K_1} \widehat{\xi}_{ik} \widehat{\phi}_k^{(1)}(t) + \sum_{l=1}^{K_2} \widehat{\zeta}_{ijl} \widehat{\phi}_l^{(2)}(t)$ for the MFPCA models. We compare these to the observed data for the same four participants shown in Figure 4. The resulting Supplemental Figures S15 and

S19 display 100 posterior samples from $\widehat{Y}_i(t)/\widehat{Y}_{ij}(t)$ (black curves) and the actual data $Y_i(t)/Y_{ij}(t)$ (red curves). The posterior samples of the smooth estimators seems to provide reasonable approximations to the observed data. Verifying how the model acts on the data is crucial, as most computation is done within exotic spaces that are hard to visualize.

6 Discussion

FPCA is one of the most popular statistical methods relying on the estimated eigenfunctions (functional principal components) of the covariance operator of a data matrix. Standard implementations of FPCA estimates the FPCs and then treats them as fixed in subsequent analysis, which may understate the observed variability and impact the interpretation of results. In this paper we propose Fast BayesFPCA, a Bayesian method treating the FPCs as parameters on the corresponding Stiefel manifold which uses posterior simulations to explore their joint distribution given the data. This is a major step forward from a both a statistical aesthetics and practical perspective.

The main idea of the approach was to represent the principal components in an orthonormal spline basis and induce a uniform prior on a linear subspace containing the smooth functions within the high dimensional Stiefel manifold that supports the eigenfunctions in the data space. This approach avoids lengthy computations required by smoothing individual functional components and re-projecting [16] or by working on the high dimensional Stiefel manifold [20].

Through visualization of the model component samples, Fast BayesFPCA provides intuition for how the model posterior surface maps to the high-dimensional Stiefel manifold geometry. These visualizations are useful for identifying potential problems, such as weak identifiability or multi-modality of the posterior distribution. Any Bayesian implementation of FPCA could, in theory, be used for this purpose. However, Fast BayesFPCA proved to be particularly easy to use for this purpose because of its simplified parameter space.

Many open questions remain including: (1) the generalizability and feasibility of these ideas for non-Gaussian outcomes; (2) theoretical guarantees and non-uniform priors on the Stiefel manifolds; (3) how these ideas interact with existing software and how methods can be further improved by exploring what is computationally feasible.

References

- [1] RePORT } RePORTER, 2024. URL https://reporter.nih.gov/search/W2pb_quLtk0En58czHh1wA/project-details/10829865.
- [2] S. L. Aronoff, K. Berkowitz, B. Shreiner, and L. Want. Glucose Metabolism and Regulation: Beyond Insulin and Glucagon. *Diabetes Spectrum*, 17(3):183–190, July 2004. ISSN 1040-9165. doi: 10.2337/diaspect.17.3.183. URL <https://dx.doi.org/10.2337/diaspect.17.3.183>. Publisher: American Diabetes Association.
- [3] S. Barua, R. A Wierchowska-McNew, N. E. P. Deutz, and A. Sabharwal. Discordance between postprandial plasma glucose measurement and continuous glucose monitoring. *The American Journal of Clinical Nutrition*, 116(4):1059–1069, Oct. 2022. ISSN 1938-3207. doi: 10.1093/ajcn/nqac181.
- [4] B. Brumback, D. Ruppert, and M. Wand. Comment on variable selection and function estimation in additive nonparametric regression using data-based prior by Shively, Kohn, and Wood. *Journal of the American Statistical Association*, 94(447):794–797, 1999.
- [5] G. Buffington. Polar Decomposition of a Matrix. Apr. 2014.
- [6] Y. Chikuse. *Statistics on Special Manifolds*, volume 174 of *Lecture Notes in Statistics*. Springer, New York, NY, 2003. ISBN 978-0-387-00160-9 978-0-387-21540-2. doi: 10.1007/978-0-387-21540-2. URL <http://link.springer.com/10.1007/978-0-387-21540-2>.
- [7] C. Crainiceanu, D. Ruppert, and M. Wand. Bayesian analysis for penalized spline regression using winbugs. *Journal of Statistical Software*, 14(14):1–24, 2005.
- [8] C. M. Crainiceanu and A. J. Goldsmith. Bayesian Functional Data Analysis Using WinBUGS. *Journal of Statistical Software*, 32:1–33, Jan. 2010. ISSN 1548-7660. doi: 10.18637/jss.v032.i11. URL <https://doi.org/10.18637/jss.v032.i11>.
- [9] C. M. Crainiceanu, J. Goldsmith, A. Leroux, and E. Cui. *Functional Data Analysis with R*. Springer New York, NY, USA, 2024.
- [10] P. Craven and G. Wahba. Smoothing noisy data with spline functions. *Numerische Mathematik*, 1:377–403, 1979.
- [11] C.-Z. Di, C. M. Crainiceanu, B. S. Caffo, and N. M. Punjabi. Multilevel functional principal component analysis. *The Annals of Applied Statistics*, 3(1): 458–488, Mar. 2009. ISSN 1932-6157, 1941-7330. doi: 10.1214/08-AOAS206.

- URL <https://projecteuclid.org/journals/annals-of-applied-statistics/volume-3/issue-1/Multilevel-functional-principal-component-analysis/10.1214/08-AOAS206.full>. Publisher: Institute of Mathematical Statistics.
- [12] FDA. Abbott Freestyle Libre Pro Summary of Safety and Effectiveness Data, Sept. 2016. URL https://www.accessdata.fda.gov/cdrh_docs/pdf15/p150021b.pdf.
- [13] A. Fisher, B. Caffo, B. Schwartz, and V. Zipunnikov. Fast, exact bootstrap principal component analysis for $p \gg 1$ million. *Journal of the American Statistical Association*, 111(514):846–860, 05 2014.
- [14] A. J. Garber. Postprandial Dysmetabolism and the Heart. *Heart Failure Clinics*, 8(4):563–573, Oct. 2012. ISSN 1551-7136. doi: 10.1016/j.hfc.2012.06.004. URL <https://www.sciencedirect.com/science/article/pii/S1551713612000566>.
- [15] J. Goldsmith, S. Greven, and C. Crainiceanu. Corrected confidence bands for functional data using principal components. *Biometrics*, 69(1):41–51, 2013.
- [16] J. Goldsmith, V. Zipunnikov, and J. Schrack. Generalized Multilevel Function-on-Scalar Regression and Principal Component Analysis. *Biometrics*, 71(2):344–353, June 2015. ISSN 0006-341X. doi: 10.1111/biom.12278. URL <https://www.ncbi.nlm.nih.gov/pmc/articles/PMC4479975/>.
- [17] S. Greven, C. Crainiceanu, B. Caffo, and D. Reich. Longitudinal functional principal component analysis. *Electronic journal of statistics*, 4:1022–1054, 2010. ISSN 1935-7524. doi: 10.1214/10-EJS575. URL <https://www.ncbi.nlm.nih.gov/pmc/articles/PMC3131008/>.
- [18] K. S. Hershon, B. R. Hirsch, and O. Odugbesan. Importance of Postprandial Glucose in Relation to A1C and Cardiovascular Disease. *Clinical Diabetes : A Publication of the American Diabetes Association*, 37(3):250–259, July 2019. ISSN 0891-8929. doi: 10.2337/cd18-0040. URL <https://www.ncbi.nlm.nih.gov/pmc/articles/PMC6640888/>.
- [19] I. James. *The Topology of Stiefel Manifolds*. Cambridge University Press, 1976.
- [20] M. Jauch, P. D. Hoff, and D. B. Dunson. Monte Carlo Simulation on the Stiefel Manifold via Polar Expansion. *Journal of Computational and Graphical Statistics*, 30(3):622–631, Sept. 2021. ISSN 1061-8600. doi: 10.1080/10618600.2020.1859382. URL <https://doi.org/10.1080/10618600.2020.1859382>. Publisher: Taylor & Francis
_eprint: <https://doi.org/10.1080/10618600.2020.1859382>.

- [21] Kai-Tai Fang and Run-Ze Li. Some methods for generating both an NT-net and the uniform distribution on a Stiefel manifold and their applications. *Computational Statistics & Data Analysis*, 24(1):29–46, Mar. 1997. ISSN 0167-9473. doi: 10.1016/S0167-9473(96)00057-6. URL <https://www.sciencedirect.com/science/article/pii/S0167947396000576>.
- [22] G. Kimeldorf and G. Wahba. A correspondence between bayesian estimation on stochastic processes and smoothing by splines. *The Annals of Mathematical Statistics*, 41(2):495–502, 1970.
- [23] K. Mardia and C. Khatri. Uniform distribution on a stiefel manifold. *Journal of Multivariate Analysis*, 7(3):468–473, 1977. ISSN 0047-259X. doi: [https://doi.org/10.1016/0047-259X\(77\)90087-2](https://doi.org/10.1016/0047-259X(77)90087-2). URL <https://www.sciencedirect.com/science/article/pii/0047259X77900872>.
- [24] T. H. Nolan, S. Richardson, and H. Ruffieux. Efficient Bayesian functional principal component analysis of irregularly-observed multivariate curves. *Computational Statistics & Data Analysis*, 203:108094, Mar. 2025. ISSN 0167-9473. doi: 10.1016/j.csda.2024.108094. URL <https://www.sciencedirect.com/science/article/pii/S0167947324001786>.
- [25] F. O’Sullivan. A statistical perspective on ill-posed inverse problems (with discussion). *Statistical Science*, 1(4):505–527, 1986.
- [26] J. Peng and D. Paul. A Geometric Approach to Maximum Likelihood Estimation of the Functional Principal Components From Sparse Longitudinal Data. *Journal of Computational and Graphical Statistics*, 18(4):995–1015, Jan. 2009. ISSN 1061-8600. doi: 10.1198/jcgs.2009.08011. URL <https://doi.org/10.1198/jcgs.2009.08011>. Publisher: ASA Website eprint: <https://doi.org/10.1198/jcgs.2009.08011>.
- [27] D. Ruppert, M. Wand, and R. Carroll. *Semiparametric Regression*. Cambridge Series in Statistical and Probabilistic Mathematics. Cambridge University Press, 2003. ISBN 9780521785167. URL <https://books.google.com/books?id=Y4uEvXFP2voC>.
- [28] M. Röhlings, T. Martin, M. Wonnemann, M. Kragl, H. H. Klein, L. Heinemann, S. Martin, and K. Kempf. Determination of Postprandial Glycemic Responses by Continuous Glucose Monitoring in a Real-World Setting. *Nutrients*, 11(10):2305, Sept. 2019. doi: 10.3390/nu11102305. URL <https://pmc.ncbi.nlm.nih.gov/articles/PMC6835966/>.
- [29] R. Shepard, S. R. Brozell, and G. Gidofalvi. The Representation and Parametrization of Orthogonal Matrices. *The Journal of Physical Chemistry A*, 119(28):7924–7939,

- July 2015. ISSN 1089-5639. doi: 10.1021/acs.jpca.5b02015. URL <https://doi.org/10.1021/acs.jpca.5b02015>. Publisher: American Chemical Society.
- [30] H. Shou, V. Zipunnikov, C. Crainiceanu, and S. Greven. Structured functional principal component analysis. *Biometrics*, 71(1):247–257, 2015.
- [31] Stan Development Team. RStan: the R interface to Stan, 2020. URL <http://mc-stan.org/>.
- [32] S. Suh and J. H. Kim. Glycemic Variability: How Do We Measure It and Why Is It Important? *Diabetes & Metabolism Journal*, 39(4):273–282, Aug. 2015. ISSN 2233-6079, 2233-6087. doi: 10.4093/dmj.2015.39.4.273. URL <http://www.e-dmj.org/journal/view.php?doi=10.4093/dmj.2015.39.4.273>. Publisher: Korean Diabetes Association.
- [33] G. Wahba. Bayesian “Confidence Intervals” for the Cross-Validated Smoothing Spline. *Journal of the Royal Statistical Society: Series B*, 45(1):133–150, 1983.
- [34] E. W. Weisstein. Legendre Polynomial. URL <https://mathworld.wolfram.com/LegendrePolynomial.html>. Publisher: Wolfram Research, Inc.
- [35] S. Wood. *Generalized Additive Models: An Introduction with R*. Chapman and Hall/CRC, 2006.
- [36] S. N. Wood. Modelling and Smoothing Parameter Estimation With Multiple Quadratic Penalties. *Journal of the Royal Statistical Society Series B: Statistical Methodology*, 62(2):413–428, July 2000. ISSN 1369-7412. doi: 10.1111/1467-9868.00240. URL <https://doi.org/10.1111/1467-9868.00240>.
- [37] J. Ye. Functional principal component models for sparse and irregularly spaced data by Bayesian inference. *Journal of Applied Statistics*, 51(7):1287–1317, May 2024. ISSN 0266-4763. doi: 10.1080/02664763.2023.2197587. URL <https://doi.org/10.1080/02664763.2023.2197587>. Publisher: Taylor & Francis eprint: <https://doi.org/10.1080/02664763.2023.2197587>.
- [38] V. Zipunnikov, B. Caffo, D. Yousem, C. Davatzikos, B. Schwartz, and C. Crainiceanu. Multilevel functional principal component analysis for high-dimensional data. *Journal of Computational and Graphical Statistics*, 20(4):852–873, 2011.

SUPPLEMENTARY MATERIAL

S1 Penalty matrix \mathbf{P}_α

We proceed by defining both of the penalty components $\mathbf{P}_0, \mathbf{P}_2$ separately, as the final penalty \mathbf{P}_α is just a linear combination of these matrices. Let $\mathbf{B}(t) = [b_1(t) | \dots | b_Q(t)]$ represent the orthonormal basis functions, such that $\mathbf{B} = \mathbf{B}(T) = [b_1(T) | \dots | b_Q(T)] \in \mathbb{R}^{M \times Q}$. First, for the zero-order penalty, \mathbf{P}_0 :

$$\mathbf{P}_0 = \frac{1}{M} \mathbf{B}^t \mathbf{B}$$

Next, the "wiggleness" penalty \mathbf{P}_2 . For this penalty, based on the squared second derivative, we introduce the second derivative matrix $\mathbf{B}'' = \mathbf{B}''(T) = [b_1''(T) | \dots | b_Q''(T)] \in \mathbb{R}^{M \times Q}$. We evaluate this matrix using the known derivatives for spline functions, but it can also be approximated numerically.

$$\mathbf{P}_2 = \frac{1}{M} (\mathbf{B}'')^t (\mathbf{B}'')$$

Combining these two penalties, we can define the linear combination \mathbf{P}_α , which will be non-degenerate when $\alpha > 0$.

$$\begin{aligned} \mathbf{P}_\alpha &= \alpha \mathbf{P}_0 + (1 - \alpha) \mathbf{P}_2 \\ &= \frac{1}{M} [\alpha \mathbf{B}^t \mathbf{B} + (1 - \alpha) (\mathbf{B}'')^t (\mathbf{B}'')] \end{aligned}$$

S2 Full conditional posteriors

As the eigenfunction and score posteriors are presented in the main text, we focus instead on the fixed effects spline coefficients w_μ , the eigenvalues λ_k , the smoothing parameters h_μ, h_k $k \in \{1, \dots, K\}$, and the noise variance σ^2 . First, for the fixed effects weights w_μ :

$$\begin{aligned}
[w_\mu | \text{others}] &\propto \prod_{i=1}^N \prod_{m=1}^M N\{Y_i(t_m) | (\mathbf{B}w_\mu)_m + \sum_{k=1}^K \xi_{ik} (\mathbf{B}\psi_k)_m, \sigma^2\} \times \exp\left(-\frac{h_\mu}{2\sigma^2} w_\mu^t \mathbf{P}_\alpha w_\mu\right) \\
&\propto \exp\left\{-\frac{1}{2\sigma^2} \sum_{i=1}^N [\mathbf{B}w_\mu - (Y_i(T) - \sum_{k=1}^K \xi_{ik} \mathbf{B}\psi_k)]^t [\mathbf{B}w_\mu - (Y_i(T) - \sum_{k=1}^K \xi_{ik} \mathbf{B}\psi_k)] - \frac{h_\mu}{2\sigma^2} w_\mu^t \mathbf{P}_\alpha w_\mu\right\} \\
&\propto \exp\left\{-\frac{1}{2\sigma^2} \sum_{i=1}^N [w_\mu^t \mathbf{B}^t \mathbf{B} w_\mu - 2(Y_i(T) - \sum_{k=1}^K \xi_{ik} \mathbf{B}\psi_k)^t \mathbf{B} w_\mu] - \frac{h_\mu}{2\sigma^2} w_\mu^t \mathbf{P}_\alpha w_\mu\right\} \\
&\propto \exp\left\{-\frac{1}{2\sigma^2} [N w_\mu^t w_\mu - 2 \sum_{i=1}^N (Y_i(T)^t \mathbf{B} w_\mu - \sum_{k=1}^K \xi_{ik} \psi_k^t \mathbf{B}^t \mathbf{B} w_\mu)] - \frac{h_\mu}{2\sigma^2} w_\mu^t \mathbf{P}_\alpha w_\mu\right\} \\
&\propto \exp\left\{-\frac{1}{2} [w_\mu^t (\frac{N \mathbf{I}_Q + h_\mu \mathbf{P}_\alpha}{\sigma^2}) w_\mu - \frac{2}{\sigma^2} \sum_{i=1}^N (Y_i(T)^t \mathbf{B} - \sum_{k=1}^K \xi_{ik} \psi_k^t) w_\mu]\right\}
\end{aligned}$$

In the above, we recognize the form of a multivariate normal distribution. The explicit parameterization is as follows:

$$[w_\mu | \text{others}] \sim MVN((N \mathbf{I}_Q + h_\mu \mathbf{P}_\alpha)^{-1} \sum_{i=1}^N [\mathbf{B}^t Y_i(T) - \sum_{k=1}^K \xi_{ik} \psi_k], \sigma^2 (N \mathbf{I}_Q + h_\mu \mathbf{P}_\alpha)^{-1})$$

While this posterior distribution is not necessarily trivial to derive, the resulting multivariate normal is relatively simple to sample given the other parameters and data.

Moving onto the eigenvalues λ_k , where IG represents the inverse gamma distribution:

$$\begin{aligned}
[\lambda_k | \text{others}] &\propto \prod_{i=1}^N N(\xi_{ik} | 0, \lambda_k) \text{IG}(\lambda_k | \alpha_\lambda, \beta_\lambda) \\
&\propto \prod_{i=1}^N \left\{ \lambda_k^{-\frac{1}{2}} \exp\left(-\frac{\xi_{ik}^2}{2\lambda_k}\right) \right\} \times \lambda_k^{-\alpha_\lambda - 1} \exp\left(-\frac{\beta_\lambda}{\lambda_k}\right) \\
&\propto \lambda_k^{-(\frac{N}{2} + \alpha_\lambda) - 1} \exp\left(-\left(\frac{1}{2} \sum_{i=1}^N \xi_{ik}^2 + \beta_\lambda\right) \times \frac{1}{\lambda_k}\right)
\end{aligned}$$

As was intended when choosing the conjugate prior, the above density has the form of the inverse-gamma. The exact parameterization is as follows:

$$[\lambda_k | \text{others}] \sim \text{IG}\left(\frac{N}{2} + \alpha_\lambda, \frac{1}{2} \sum_{i=1}^N \xi_{ik}^2 + \beta_\lambda\right)$$

Consider next the smoothing parameters h_μ, h_k for $k \in \{1, 2, \dots, K\}$. We derive the posterior for h_μ first:

$$\begin{aligned} [h_\mu | \text{others}] &\propto \exp\left(-\frac{h_\mu}{2\sigma^2} w_\mu^t \mathbf{P}_\alpha w_\mu\right) \times \Gamma(\alpha_\mu, \beta_\mu) \\ &\propto \exp\left(-\frac{h_\mu}{2\sigma^2} w_\mu^t \mathbf{P}_\alpha w_\mu\right) \times h_\mu^{\alpha_\mu - 1} \exp(-\beta_\mu h_\mu) \\ &\propto h_\mu^{\alpha_\mu - 1} \exp\left(-\left(\frac{w_\mu^t \mathbf{P}_\alpha w_\mu}{2\sigma^2} + \beta_\mu\right) h_\mu\right) \end{aligned}$$

One can recognize the form of the gamma distribution in the last line above, leading to the conditional posterior $[h_\mu | \text{others}] \sim \Gamma(\alpha_\mu, \frac{w_\mu^t \mathbf{P}_\alpha w_\mu}{2\sigma^2} + \beta_\mu)$. We can similarly derive the conditional posterior for the general eigenfunction smoothing parameter h_k :

$$\begin{aligned} [h_k | \text{others}] &\propto \exp\left(-\frac{h_k}{2\sigma^2} \psi_k^t \mathbf{P}_\alpha \psi_k\right) \times \Gamma(\alpha_\psi, \beta_\psi) \\ &\propto \exp\left(-\frac{h_k}{2\sigma^2} \psi_k^t \mathbf{P}_\alpha \psi_k\right) \times h_k^{\alpha_\psi - 1} \exp(-\beta_\psi h_k) \\ &\propto h_k^{\alpha_\psi - 1} \exp\left(-\left(\frac{\psi_k^t \mathbf{P}_\alpha \psi_k}{2\sigma^2} + \beta_\psi\right) h_k\right) \end{aligned}$$

Once more, the form of the gamma distribution is clear in the final line above, leading to the conditional posterior $[h_k | \text{others}] \sim \Gamma(\alpha_\psi, \frac{\psi_k^t \mathbf{P}_\alpha \psi_k}{2\sigma^2} + \beta_\psi)$.

We move on finally to the conditional posterior of the noise variance σ^2 :

$$\begin{aligned} [\sigma^2 | \text{others}] &\propto \prod_{i=1}^N \prod_{m=1}^M N(Y_i(t_m) | (\mathbf{B}w_\mu)_m + \sum_{k'=1}^K \xi_{ik'} (\mathbf{B}\psi_{k'})_m, \sigma^2) \times \\ &\quad \exp\left(-\frac{h_\mu}{2\sigma^2} w_\mu^t \mathbf{P}_\alpha w_\mu\right) \times \exp\left(-\frac{1}{2\sigma^2} \sum_{k=1}^K h_k \psi_k^t \mathbf{P}_\alpha \psi_k\right) \times \text{IG}(\sigma^2 | \alpha_\sigma, \beta_\sigma) \\ &\propto \prod_{i=1}^N \prod_{m=1}^M (\sigma^2)^{-\frac{1}{2}} \exp\left(-\frac{\{Y_i(t_m) - [(\mathbf{B}w_\mu)_m + \sum_{k'=1}^K \xi_{ik'} (\mathbf{B}\psi_{k'})_m]\}^2}{2\sigma^2}\right) \times \\ &\quad \exp\left(-\frac{h_\mu}{2\sigma^2} w_\mu^t \mathbf{P}_\alpha w_\mu\right) \times \exp\left(-\frac{1}{2\sigma^2} \sum_{k=1}^K h_k \psi_k^t \mathbf{P}_\alpha \psi_k\right) \times (\sigma^2)^{-\alpha_\sigma - 1} \exp\left(-\frac{\beta_\sigma}{\sigma^2}\right) \end{aligned}$$

For the sake of simplicity and brevity, we define the residual quantity $Q_{im} = Y_i(t_m) - \{(\mathbf{B}w_\mu)_m + \sum_{k'=1}^K \xi_{ik'} (\mathbf{B}\psi_{k'})_m\}$. Proceeding from here:

$$\begin{aligned}
[\sigma^2|\text{others}] &\propto (\sigma^2)^{-\left(\frac{NM}{2}+\alpha_\sigma\right)-1} \exp\left(-\frac{\sum_{i=1}^N \sum_{m=1}^M Q_{im}^2}{2\sigma^2}\right) \times \exp\left(-\frac{h_\mu w_\mu^t \mathbf{P}_\alpha w_\mu}{2\sigma^2}\right) \times \\
&\exp\left(-\frac{1}{2\sigma^2} \sum_{k=1}^K h_k \psi_k^t \mathbf{P}_\alpha \psi_k\right) \times \exp\left(-\frac{\beta_\sigma}{\sigma^2}\right) \\
&\propto (\sigma^2)^{-\left(\frac{NM}{2}+\alpha_\sigma\right)-1} \exp\left(-\frac{1}{2\sigma^2} \left[\sum_{i=1}^N \sum_{m=1}^M Q_{im}^2 + h_\mu w_\mu^t \mathbf{P}_\alpha w_\mu + \sum_{k=1}^K h_k \psi_k^t \mathbf{P}_\alpha \psi_k + 2\beta_\sigma \right]\right)
\end{aligned}$$

The last line above is clearly the form of the inverse gamma distribution, with exact parameterization as follows:

$$[\sigma^2|\text{others}] \sim \text{IG}\left(\frac{NM}{2} + \alpha_\sigma, \frac{1}{2} \left[\sum_{i=1}^N \sum_{m=1}^M Q_{im}^2 + h_\mu w_\mu^t \mathbf{P}_\alpha w_\mu + \sum_{k=1}^K \psi_k^t \mathbf{P}_\alpha \psi_k + 2\beta_\sigma \right]\right)$$

S3 Simulations

S3.1 General information

All code used for data simulation and subsequent model fitting can be found at this [GitHub repository](#). We compare the simulation bases with those extracted from the real data in Figure S1.

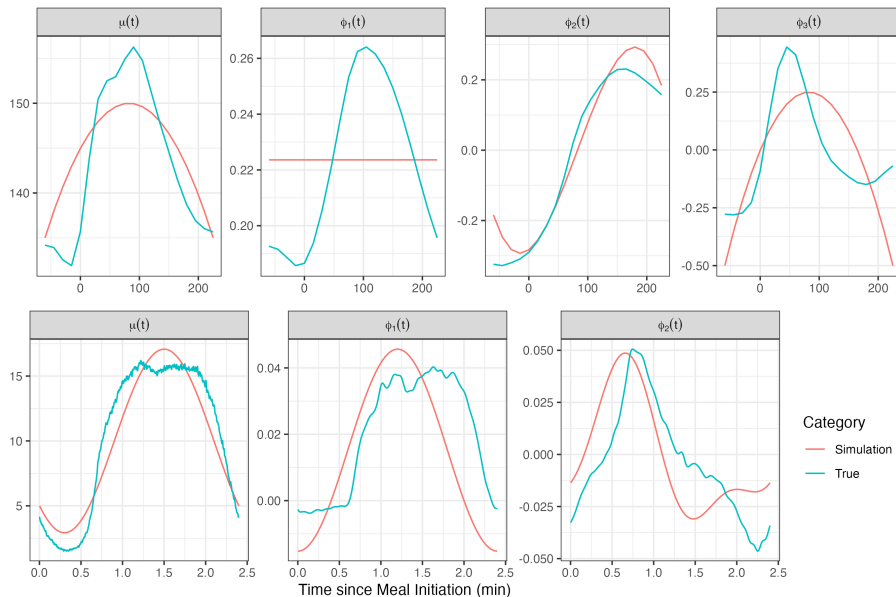


Figure S1: Comparison between functional forms used in simulations (red) and the estimates from fitting FPCA to the actual data (blue) for the two simulation scenarios. The first row corresponds to the CGM scenario, based upon the by-participant mean post-prandial CGM curves from the DASH4D study. The second row corresponds to the physical activity (PA) scenario, based upon mean MIMS data from the 2014 wave of NHANES accelerometry data.

S3.2 $M = 60$ Extension

When sampling along the functional domain more frequently ($M = 60$ rather than $M = 30$), simulation results remain qualitatively the same. Figure S2 indicates that FAST is largely non-inferior to GFSR and SVD-GP with regards to accuracy of posterior estimates of the functional components.

Figure S3 indicates that FAST achieves nominal posterior coverage of the functional components, which is not the case for GFSR nor SVD-GP.

This contrast in coverage extends to the scores, as can be observed in Figure S4.

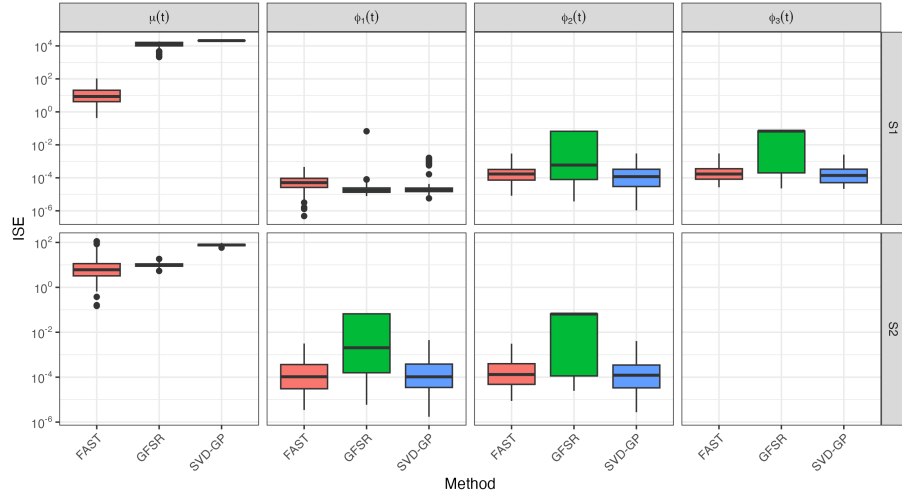


Figure S2: Boxplots of the ISE for the mean and eigenfunctions for FAST (red), GFSR (green), and SVD-GP (blue). First row: S1; second row: S2. Each column: mean or corresponding eigenfunction. Y-axis is on the log scale for presentation purposes. Results shown for $N = 50$ functions with $M = 60$ observations per function.

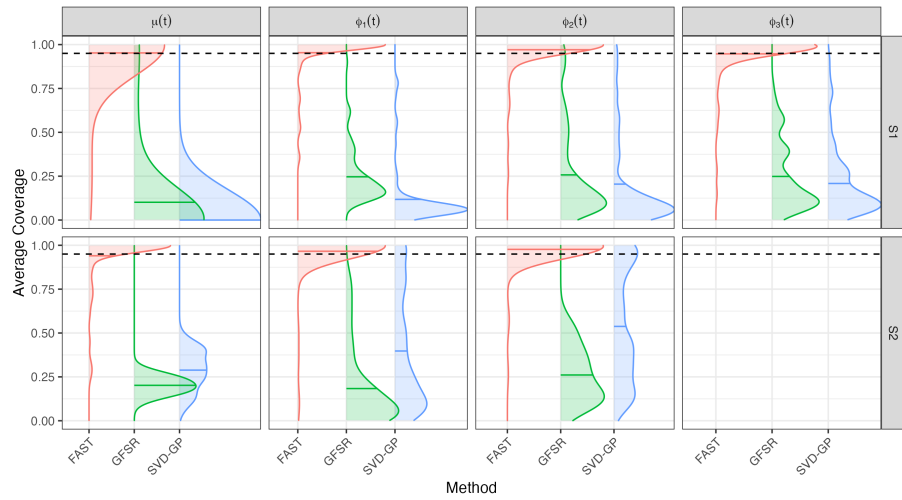


Figure S3: Kernel smoother of coverage probabilities of 95% credible intervals of the true mean and eigenfunctions for FAST (red), GFSR (green), and SVD-GP (blue). First row: S1; second row: S2. Each column: corresponding function. Distribution means: horizontal solid lines; nominal 95% level: horizontal dotted lines. Results shown for $N = 50$ functions with $M = 60$ observations per function.

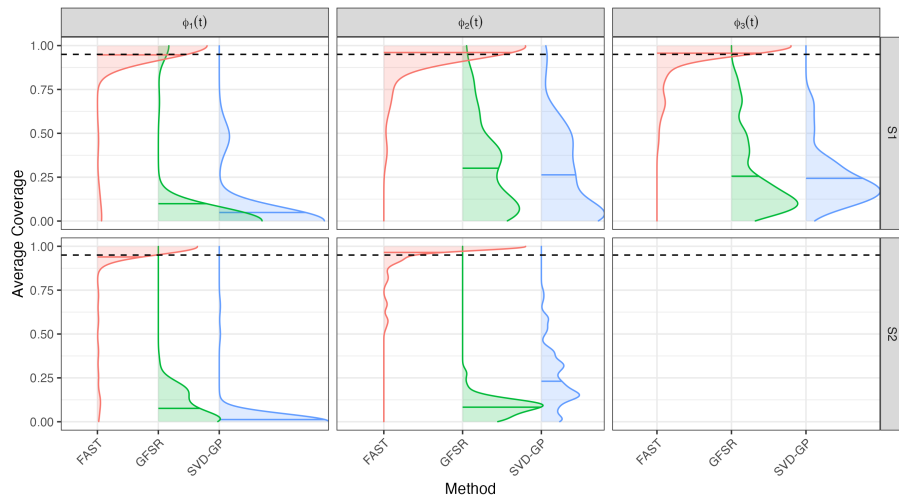


Figure S4: Kernel smoother of coverage probabilities of 95% credible intervals of the true scores, ξ_{ik}^b , for FAST (red), GFSR (green), and SVD-GP (blue). First row: S1; second row: S2. Each column: corresponding eigenfunction. Distribution means: horizontal solid lines; nominal 95% level: horizontal dotted lines. Results shown for $N = 50$ functions with $M = 60$ observations per function.

S3.3 Multilevel extension

We performed a simple 2-level simulation study to assess performance of the multilevel extension of FAST. This simulation includes 50 groups at the first level ($N = 50$), each with 5 functional observations ($\forall i, J_i = 5$) for a total of 250 functions. We were only able to compare against the GFSR approach for this simulation, as SVD-GP has no available multilevel extension. We based our study around the Fourier basis, a commonly known set of orthogonal functional bases on $t \in [0, 1]$. Here again, we apply appropriate scaling to ensure that the discretely-observed functions remain orthonormal, and we let $f_k(\cdot)$ represent Legendre polynomial of order k rescaled to $[0, 1]$ [34].

Multilevel Scenario

$$\begin{aligned} \phi_k^{(1)}(t) &= \left\{ \sqrt{\frac{2}{M}} \sin(2\pi t), \sqrt{\frac{2}{M}} \cos(2\pi t) \right\}; & \lambda_k^{(1)} &= \{10000, 2000\} \\ \phi_l^{(2)}(t) &= \left\{ \sqrt{\frac{2}{M}} \sin(4\pi t), \sqrt{\frac{2}{M}} \cos(4\pi t) \right\}; & \lambda_l^{(2)} &= \{8000, 4000\} \\ \mu(t) &= 5f_1(t) - 3f_2(t); & \sigma^2 &= 16 \end{aligned}$$

We first present the integrated squared error (ISE) of the functional components $\mu(t)$, $\phi_k^{(1)}(t)$, $\phi_l^{(2)}(t)$ in Figure S5. We calculate this measure using the same procedure detailed in Section 4. Each panel corresponds to one of the functional components, ordered from the population mean to the second level eigenfunctions. We place these plots on the log scale for presentation, as the fixed effects and eigenfunction errors are at different scales.

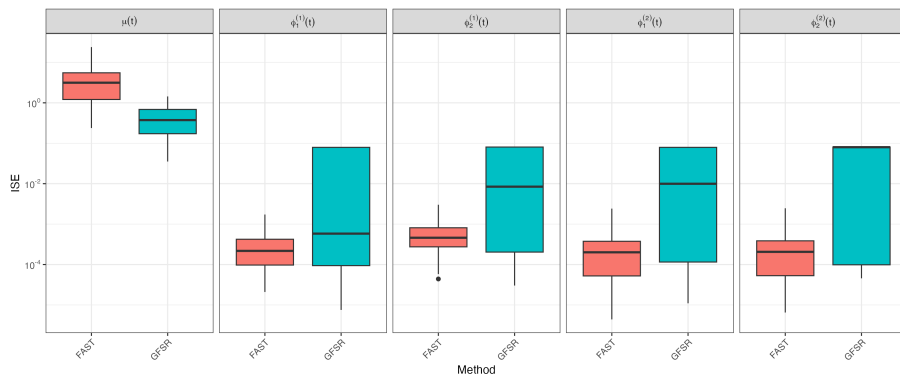


Figure S5: Boxplots of the ISE for the mean and eigenfunctions for FAST (red) and GFSR (blue) from the multilevel simulations. Y-axis is on the log scale for presentation purposes.

Figure S5 seems to indicate that GFSR has lower ISE for the fixed effects mean $\mu(t)$, but often produces much poorer posterior estimates of the eigenfunctions at both levels.

We next consider the coverage of these functional components by the point-wise equal-tailed 95% credible intervals produced by FAST and GFSR. As in Section 4, we estimate coverage probability using the proportion of time points which are covered for each simulated dataset, visualizing the result with a kernel smooth in Figure S6. We include on

this Figure the mean of each coverage distribution (horizontal solid lines) and the nominal coverage 95% coverage level (horizontal dotted lines).

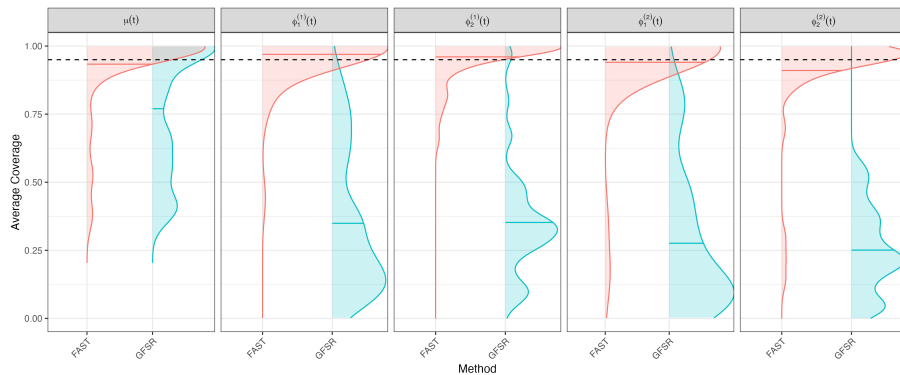


Figure S6: Kernel smoother of coverage probabilities of 95% credible intervals of the true mean and eigenfunctions for FAST (red) and GFSR (blue) from the multilevel simulations. Each column: corresponding function. Distribution means: horizontal solid lines; nominal 95% level: horizontal dotted lines.

Similar to the single-level simulations, we find that only FAST produces nearly nominal coverage of the true underlying functional components. The GFSR mean coverages range from ≈ 0.27 to ≈ 0.76 .

This disparity in coverage extends to the scores at both levels, ξ_{ik} and ζ_{ijk} , as can be observed in Figure S7. We estimate score coverage in the same fashion illustrated in Section 4. For each simulated dataset $b \leq B$, we calculate the 95% credible intervals for each individual $\xi_{ik}^b, \zeta_{ijk}^b$ from the posterior samples. We then estimate the coverage probability by aggregating the coverage indicators by the corresponding eigenfunction. Figure S7 visualizes the kernel smooths of the corresponding vectors of coverage, complete with distribution mean (solid horizontal lines) and nominal level (dashed horizontal lines). As was the case for the functional components presented in Figure S6, nominal coverage of the scores is uniquely achieved by FAST. GFSR, on the other hand, achieves mean coverages between ≈ 0.15 and ≈ 0.6 .

S3.4 Computation time comparison

We first present Table S1 summarizing the time taken by each of the three methods (FAST, GFSR, and SVD-GP) to complete the main simulation scenarios on a personal laptop. Results indicate that FAST tends to be 2-4 times faster in every case than the two comparator methods, with differences changing based upon the value of M .

To further explore how each of the three methods scale with the number of time series N and number of observations along the functional domain M , we fit multiple scaled-up instances of simulation scenario S1 on the same personal machine. We first fixed $N = 50$

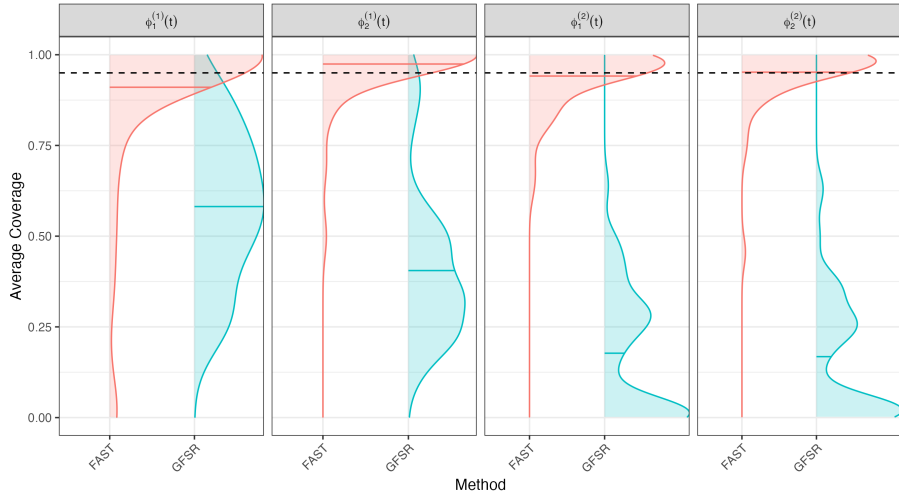


Figure S7: Kernel smoother of coverage probabilities of 95% credible intervals of the true scores, $\xi_{ik}^b, \zeta_{ijk}^b$, for FAST (red) and GFSR (blue) from the multilevel simulations. Each column: corresponding eigenfunction. Distribution means: horizontal solid lines; nominal 95% level: horizontal dotted lines.

Simulation		Timing (s, Mean [Min., Max.])		
Scenario	M	FAST	GFRS	SVD-GP
S1	30	60.7 [56.2, 68.0]	258.0 [246.4, 277.7]	122.2 [111.2, 150.3]
S1	60	90.0 [78.0, 112.0]	341.7 [326.9, 363.6]	276.5 [255.9, 303.4]
S2	30	42.7 [31.6, 67.4]	137.6 [121.5, 150.5]	116.7 [106.9, 142.6]
S2	60	53.4 [43.3, 75.5]	170.8 [161.4, 178.8]	277.8 [269.5, 293.6]

Table S1: Table of computational times, listing first the mean and then the range from minimum to maximum, for each combination of scenario, M value, and method.

and scaled $M = 30, 60, 100, 200, 300$, with the results present in Figure S8. From this figure, it is clear that SVD-GP scales super-linearly with the number of observations M .

We also fixed $M = 30$ and scaled $N = 50, 100, 200, 300$, visualizing the results in Figure S9. This figure indicates that GFSR scales super-linearly with the number of functions N .

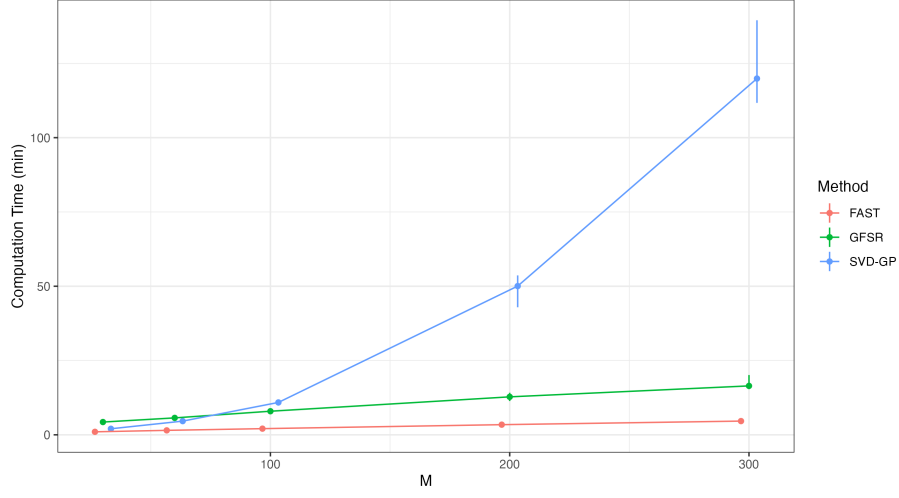


Figure S8: Computational time taken for the various methods as the number of observations along the domain M grows larger, comparing FAST (red), GFSR (green), and SVD-GP (blue).

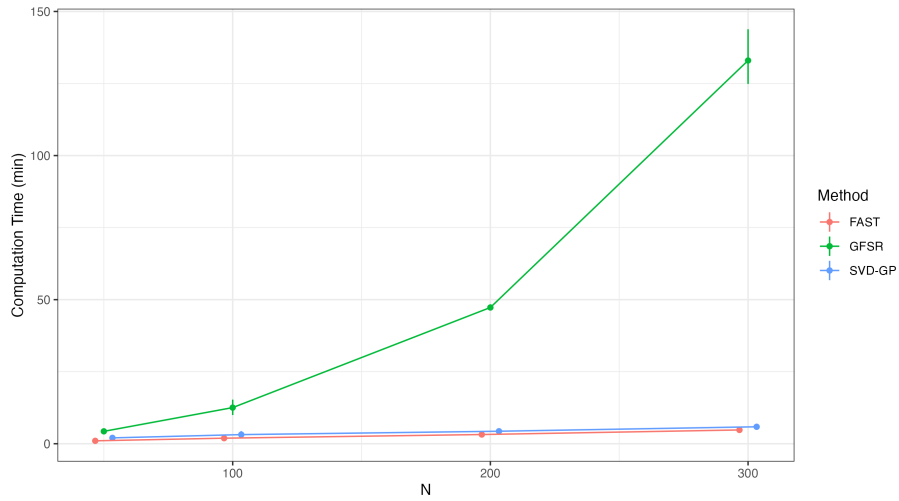


Figure S9: Computational time taken for the various methods as the number of functions observed N grows larger, comparing FAST (red), GFSR (green), and SVD-GP (blue).

S4 Bayesian FPCA of randomly-chosen CGM within diets

As an alternative single-level analysis, we randomly sample a function for each participant within each diet rather than aggregating. These functions each represent a single instantiation of the meal process for that participant within the particular diet, whereas the aggregate functions analyzed in Section 5.3 have varying levels of noise based upon the number of curves included in the average. However, when performing the by-diet FPCA analyses on these randomly chosen curves instead of the aggregated CGM, we observe qualitatively identical results. We first present the eigenfunctions with associated uncertainty in Figure S10. The primary difference we observe is in the additional sampling variability of $\hat{\phi}_1(t)$ for the DASH, Lower Sodium diet, along with some of the posterior samples having greater curvature. This is indicative of differences in mean mealtime glucose being much lower for this population, reduced to be on similar scale to differences peakedness.

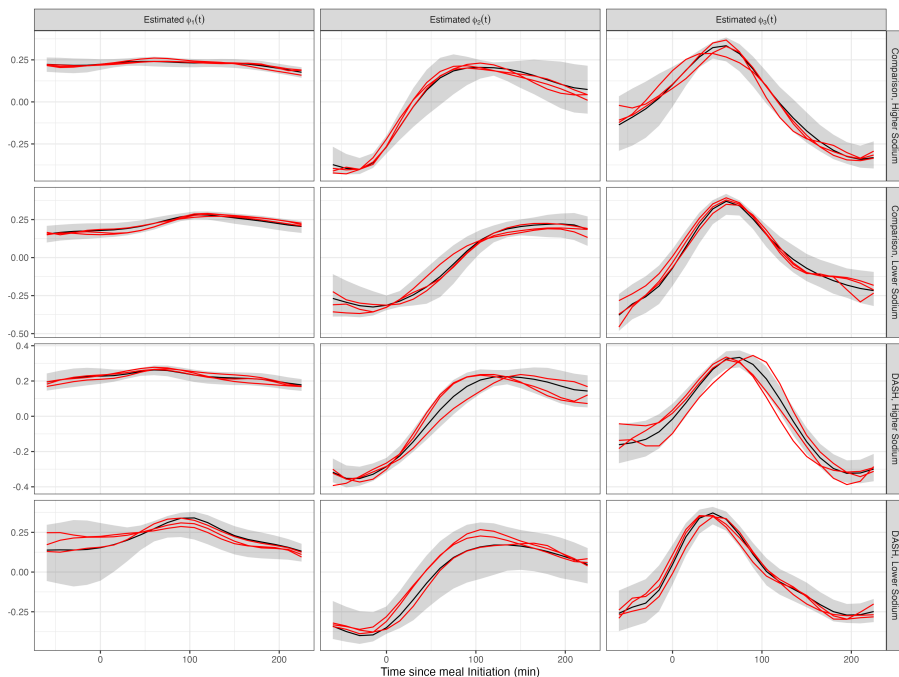


Figure S10: Bayesian FPCA results for the first three PCs (each column corresponds to one FPC) for each of the four diets (each row corresponds to one diet). X-axis: time from the start of the meal. Black curves: posterior mean; red curves: three samples from the posterior of the PCs; shaded areas: pointwise 95% credible intervals.

We present also the corresponding eigenvalues in Figure S11, where again one observes the uniqueness of the DASH, Lower Sodium diet. In this analysis as well, there is lower overall variability for this diet (assessed by sum of eigenfunctions). Further, this difference is again driven by the first eigenvalue/eigenfunction pair in this analysis.

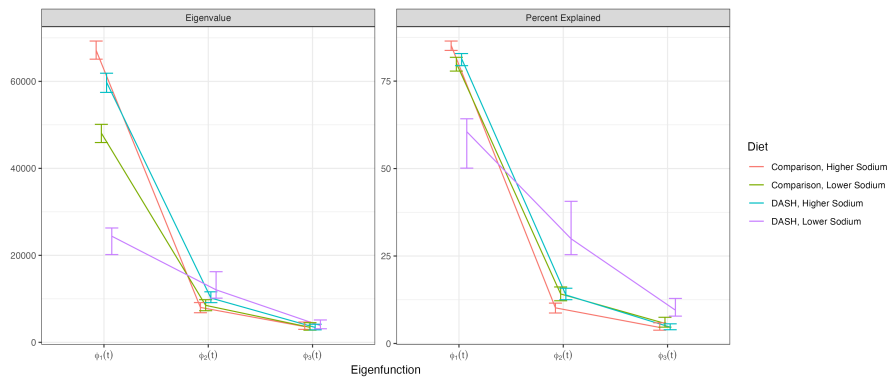


Figure S11: Eigenvalue and percent-variability estimates from the Bayesian FPCA models fit to each of the four diets (each line and color corresponds to one diet). X-axis: eigenfunction corresponding to eigenvalue/percent variance explained. All estimates are presented with their corresponding 95% credible intervals.

S5 Bayesian FPCA of average CGM within diets

In this section, we provide the monitoring figures produced to ensure that the analyses in Section 5.3 achieved convergence. Figures S12, S13, and S14 all present trace plots of the eigenfunction evaluations at particular points along the temporal domain ($t = 15, 105$ and 210 minutes relative to the start of the meal). These figures indicate effective mixing of the chains with minimal autocorrelation, providing evidence for convergence.

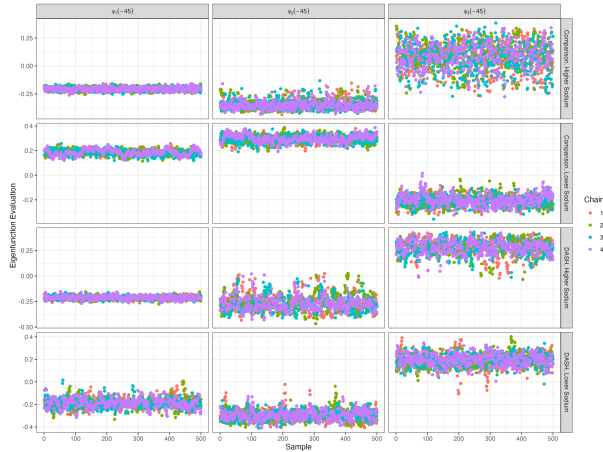


Figure S12: Trace plots displaying samples of $\phi_k(t)$ evaluated at $t = -45$ minutes relative to meal intake, where coloration indicates sampling chain

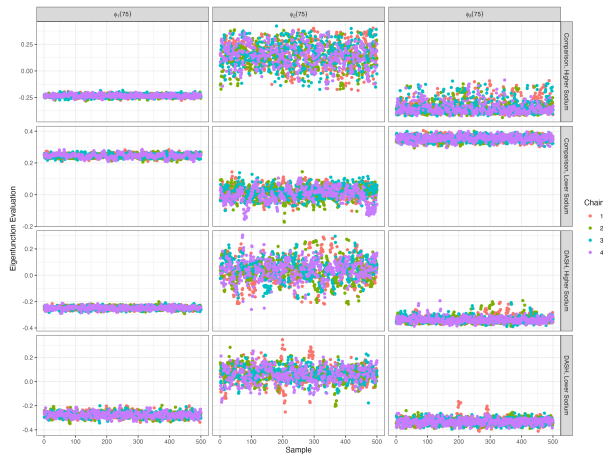


Figure S13: Trace plots displaying samples of $\phi_k(t)$ evaluated at $t = 75$ minutes relative to meal intake, where coloration indicates sampling chain.

We also visualized samples of the smooth curves at the data level in Figure S15. This figure was generated to assess whether our models represent the single-level data well throughout sampling. Figure S15 provides supporting evidence for this fact, as all raw data curves are approximated well by the smooth samples.

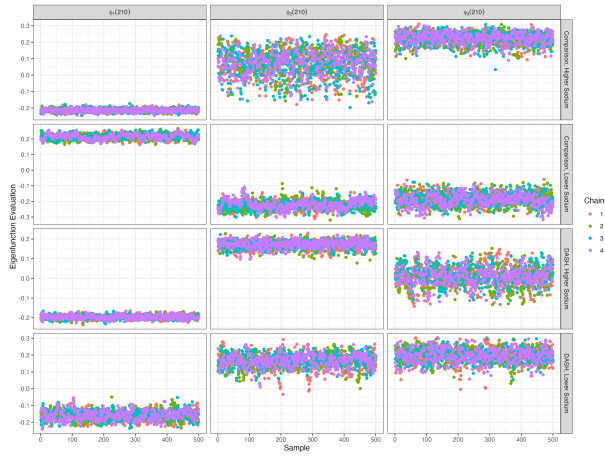


Figure S14: Trace plots displaying samples of $\phi_k(t)$ evaluated at $t = 210$ minutes relative to meal intake, where coloration indicates sampling chain

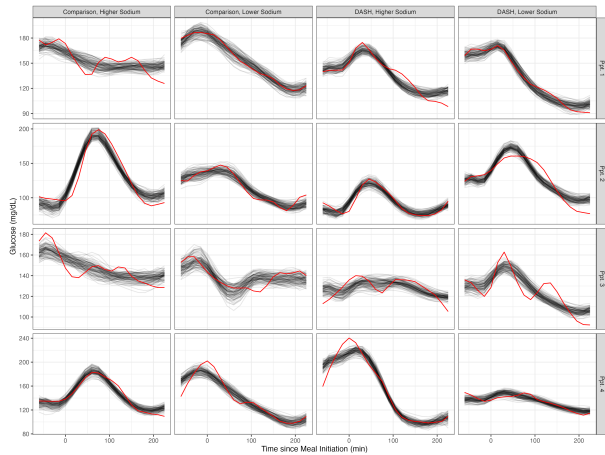


Figure S15: Visualization of samples from randomly selected underlying smooths $\hat{Y}_i(t) = \mu(t) + \sum_{k=1}^K \xi_{ik} \phi_k(t)$ from each FPCA model, with the original data $Y_i(t)$ overlaid. The black curves indicate samples, while the red curves correspond to the original data.

S6 Bayesian MFPCA of individual CGM curves

In this section, we provide the monitoring figures produced to ensure that the analyses in Section 5.4 achieved convergence. Figures S16, S17, and S18 all present trace plots of the eigenfunction evaluations at particular points along the temporal domain ($t = 15, 105$ and 210 minutes relative to the start of the meal). These figures indicate effective mixing of the chains with minimal autocorrelation, providing evidence for convergence.



Figure S16: Trace plots evaluating samples of $\phi_k^{(1)}(t), \phi_l^{(2)}(t)$ at $t = -45$ minutes relative to meal intake, where coloration indicates sampling chain.



Figure S17: Trace plots evaluating samples of $\phi_k^{(1)}(t), \phi_l^{(2)}(t)$ at $t = 75$ minutes relative to meal intake, where coloration indicates sampling chain.

We also visualized samples of the smooth curves at the data level in Figure S19. This figure was generated to assess whether our models represent the multi-level data well throughout sampling. Figure S19 provides supporting evidence for this fact, as all raw data curves are approximated well by the smooth samples.



Figure S18: Trace plots evaluating samples of $\phi_k^{(1)}(t), \phi_l^{(2)}(t)$ at $t = 210$ minutes relative to meal intake, where coloration indicates sampling chain.

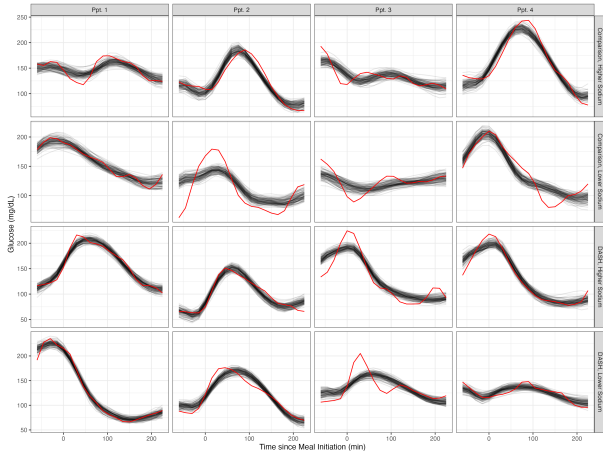


Figure S19: Visualization of samples from randomly selected underlying smooths $\hat{Y}_{ij}(t)$ from the fitted MFPCA model, with the original data $Y_{ij}(t)$ overlaid. The black curves indicate samples, while the red curves correspond to the original data.